

# JGR Solid Earth

## RESEARCH ARTICLE

10.1029/2022JB025443

### Special Section:

Understanding and anticipating Induced Seismicity: from mechanics to seismology

### Key Points:

- A stimulation strategy for Enhanced Geothermal System, called pore pressure preconditioning, is introduced
- Preconditioning results in early time dynamic rupture being contained or suppressed by the induced stress- and fracture-energy- barrier
- With sufficient preconditioning, the slipping patch must surpass the induced pressure barrier before nucleating runaway dynamic rupture

### Correspondence to:

B. Fryer,  
[barnaby.fryer@epfl.ch](mailto:barnaby.fryer@epfl.ch)

### Citation:

Fryer, B., Lebihain, M., & Violay, M. (2023). Single-well pore pressure preconditioning for Enhanced Geothermal System stimulation. *Journal of Geophysical Research: Solid Earth*, 128, e2022JB025443. <https://doi.org/10.1029/2022JB025443>

Received 19 AUG 2022

Accepted 11 FEB 2023

### Author Contributions:

**Conceptualization:** Barnaby Fryer, Mathias Lebihain

**Data curation:** Barnaby Fryer

**Formal analysis:** Barnaby Fryer, Mathias Lebihain, Marie Violay

**Funding acquisition:** Marie Violay

**Investigation:** Barnaby Fryer

**Methodology:** Barnaby Fryer, Mathias Lebihain

**Project Administration:** Marie Violay

**Resources:** Marie Violay

**Software:** Mathias Lebihain

© 2023 The Authors.

This is an open access article under the terms of the [Creative Commons Attribution-NonCommercial License](https://creativecommons.org/licenses/by-nc/4.0/), which permits use, distribution and reproduction in any medium, provided the original work is properly cited and is not used for commercial purposes.

## Single-Well Pore Pressure Preconditioning for Enhanced Geothermal System Stimulation

Barnaby Fryer<sup>1</sup> , Mathias Lebihain<sup>2</sup> , and Marie Violay<sup>1</sup> 

<sup>1</sup>Laboratory of Experimental Rock Mechanics, École Polytechnique Fédérale de Lausanne, Lausanne, Switzerland,

<sup>2</sup>Laboratoire Navier, CNRS (UMR 8205), École des Ponts ParisTech, Université Gustave Eiffel, Champs-sur-Marne, France

**Abstract** The stress state is an important parameter in terms of both earthquake nucleation and rupture. Here, a new stimulation technique is proposed for Enhanced Geothermal Systems (EGSs), which have previously been burdened with a number of high-profile incidences of induced seismicity. This stimulation technique pre-emptively alters, or preconditions, the stress state before injection. This preconditioning is achieved through fluid production, such that the zone of reduced pore pressure around the well results in a stress- and fracture-energy- barrier to potential nucleating and/or propagating ruptures near the point of injection. Using an existing 1-D linear slip-weakening model, it is shown how this methodology has the potential to either suppress the nucleation of dynamic events or halt their propagation. In particular, reducing the pore pressure around the region to be stimulated such that the residual shear stress rises above the in-situ value of shear stress results in ultimately stable nucleation regimes. These results hold for injection times which are small compared to the required time of production, but this methodology results in nucleation lengths, or, analogously, stimulated areas, which are orders of magnitudes larger than those safely achievable without preconditioning. An example of how this approach may be applied in the field as well as other possible methods to achieve a preconditioned reservoir are provided. Both laboratory-scale and meso-scale testing of preconditioning are recommended to further constrain the applicability of this methodology for the creation of EGSs.

**Plain Language Summary** Enhanced Geothermal Systems (EGSs) are attractive due to their ability to provide potentially ubiquitous clean baseload power. However, they have been shown to be capable of inducing damaging and dangerous earthquakes, especially during and just after reservoir stimulation, a process enhancing the ease of fluid flow and required if these systems are to achieve sufficient energy fluxes. Interestingly, the state of stress is an important parameter for earthquake behavior. As previous studies have shown that engineers are able to influence the state of stress through their operations, a methodology is proposed that pre-emptively alters, or preconditions, the stress field through the reduction of pressure before stimulation. The possible effects of this type of preconditioning are investigated by building upon a previously developed numerical model. The results indicate that pore pressure preconditioning may be able to delay the nucleation of an earthquake or stop an already-nucleated earthquake from growing larger, meaning it may allow for reservoir stimulation at a reduced risk of induced seismicity. This methodology can be performed with a single well but requires large production times when compared to the time of injection. Laboratory-scale and medium-scale testing of this methodology are recommended before its application to a real EGS.

## 1. Introduction

The stress state in the subsurface has been shown to be an important parameter for a wide variety of considerations related to seismicity, both natural and anthropogenic. It is characterized for a fault embedded in the subsurface by the shear stress acting along and the total stress acting normal to the plane of the fault. The effective normal stress acting on the fault is then defined as total normal stress minus the contribution of pore pressure. The reactivation of a locked fault is controlled by the ratio of the shear to the effective normal stress acting on the fault plane, as generally dictated by the Mohr-Coulomb criterion. Upon reactivation, slip can either be characterized as seismic or aseismic (i.e., with or without the notable radiation of seismic waves) in nature, depending in large part on the stress state (e.g., Harbord et al., 2017; Leeman et al., 2016; Okubo & Dieterich, 1984; Passelègue et al., 2019). Further, the propagation of the rupture fronts of these slip events can be halted by heterogeneous stress barriers along the fault, as observed on both natural-scale (Gupta & Scholz, 2000; Hussein et al., 1975; Lay & Kanamori, 1981; Sibson, 1985) and laboratory-scale (Bayart et al., 2018; Ke et al., 2018, 2021; Wu &

**Supervision:** Mathias Lebihain, Marie Violay

**Validation:** Barnaby Fryer, Mathias Lebihain

**Visualization:** Barnaby Fryer

**Writing – original draft:** Barnaby Fryer

**Writing – review & editing:** Barnaby Fryer, Mathias Lebihain, Marie Violay

McLaskey, 2018) faults as well as predicted theoretically (Ampuero et al., 2006; Hussein et al., 1975). This arrest occurs because propagation of a seismic rupture depends on the local fracture energy, itself a function of the stress along the fault plane, and the global stress drop profile along the fault which provides energy to the propagating rupture tip (Bayart et al., 2016, 2018; Cebry et al., 2022; Freund, 1998; Galis et al., 2017; Gvirtzman & Fineberg, 2021; Hussein et al., 1975; Kammer et al., 2015; Pagliarunga et al., 2022).

Industrial reservoir-engineering operations have been shown to be capable of influencing the subsurface state of stress, as most notably evidenced by production-induced and injection-induced seismicity related to pore pressure increase (Healy et al., 1968; Raleigh et al., 1976), poroelasticity (e.g., Segall, 1989; Segall & Lu, 2015; Suckale, 2009), thermoelasticity (e.g., Kwiatek et al., 2015; Rutqvist et al., 2016), and stress redistribution (e.g., Catalli et al., 2013, 2016). This has also been shown by hydraulic fracturing operations through stress shadowing (e.g., Fisher et al., 2004; Vermilyen & Zoback, 2011) and altered fracture geometries related to prior fluid injection and production (e.g., Berchenko & Detournay, 1997; Elbel & Mack, 1993; Gao et al., 2019; Minner et al., 2002).

The recognized significance of the stress state for many industrial operations as well as operators' proven ability to influence it, has led to the notion that the stress state can be intentionally preconditioned before an operation to that operation's eventual benefit. The idea of preconditioning was first introduced by the mining industry in the late 1950s as a way to improve rockburst conditions in mines, by blasting to relieve stress in near-face regions (Roux et al., 1957; Toper et al., 2000). In the petroleum industry, reservoir-engineering solutions which involve the manipulation of the stress field have been proposed since the 1970s (Shuck, 1977). Initially, these proposals were exclusively focused on mode-I hydraulic fracturing and were related to the altering of the stress field such that a hydraulic fracture would either be oriented in a different direction (Shuck, 1977; Warpinski & Branagan, 1989), directed toward a desired location (Bouteca et al., 1983), or have its containment ensured within a production reservoir (van Eekelen, 1982). More recently, a stress preconditioning technique called microseismic-depletion delineation has been developed and applied to field-scale hydraulic fracturing operations (Dohmen et al., 2013, 2014, 2017; Norbeck & Horne, 2015).

Enhanced Geothermal Systems (EGSs), while offering the attractive possibility of providing renewable baseload power, have been plagued by a number of instances of high-profile induced seismicity, most notably in Basel, Switzerland (Häring et al., 2008) and Pohang, South Korea (Grigoli et al., 2018; Kim et al., 2018). This has led to the realization that the development of new reservoir stimulation techniques is crucial for the development of EGS (Baria et al., 2004; Häring et al., 2008), with the recognition of the importance of injection strategy (Ciardo & Rinaldi, 2022; Gischig, 2015) and a number of stimulation strategies already being proposed (Baria et al., 2004; Cornet, 2019; Fryer et al., 2020; Hofmann et al., 2018; Zang et al., 2013; Zimmermann et al., 2010), albeit with limited success up to this point (e.g., Hofmann et al., 2019; Noël et al., 2019). For the moment, the preconditioning of the stress field as applied in the mining and oil and gas industries has rarely been suggested (Fryer et al., 2020) and has not yet been applied to an EGS, despite the adoption of a number of other oil and gas technologies such as directional drilling (e.g., Kim et al., 2018; Kwiatek et al., 2008; Norbeck et al., 2018; Tester et al., 2006) and multi-stage well stimulation (Kumar & Ghassemi, 2019; Meier et al., 2015), as well as the general recognition that the adoption of techniques from the oil and gas industry is critical for the development of EGS (Häring et al., 2008).

EGS stimulation is generally assumed to occur in shear (e.g., Evans, Genter, & Sausse, 2005; Evans, Moriya, et al., 2005) due to shear-induced dilatancy (e.g., Lee & Cho, 2002), albeit with certain instances thought to be more related to mode-I opening (e.g., McClure & Horne, 2014). If it can be assumed that EGS stimulation depends on inducing slip along a shear fracture, understanding what conditions cause a fault to slip aseismically as opposed to dynamically becomes a highly relevant question.

Here, a new form of pore-pressure, or effective-normal-stress, preconditioning is proposed. The proposal consists of a well drilled into a fault. This well is used to produce fluid from the fault, reducing the fluid pressure and thereby increasing the effective normal stress along the fault. Following this, high-pressure injection is performed to stimulate the fault, resulting in its reactivation. Slip is proposed to begin near the well due to the increased fluid pressure, but the nucleation of a runaway dynamic event is proposed to either be halted or delayed, depending on background stress and injection pressure, by the zone of increased normal stress in front of the nucleating event caused by the prior fluid production, in a similar fashion to how dilatancy-induced pore pressure barriers have been shown to result in stable slip or arrested rupture on otherwise unstable faults (Ciardo & Lecampion, 2019;

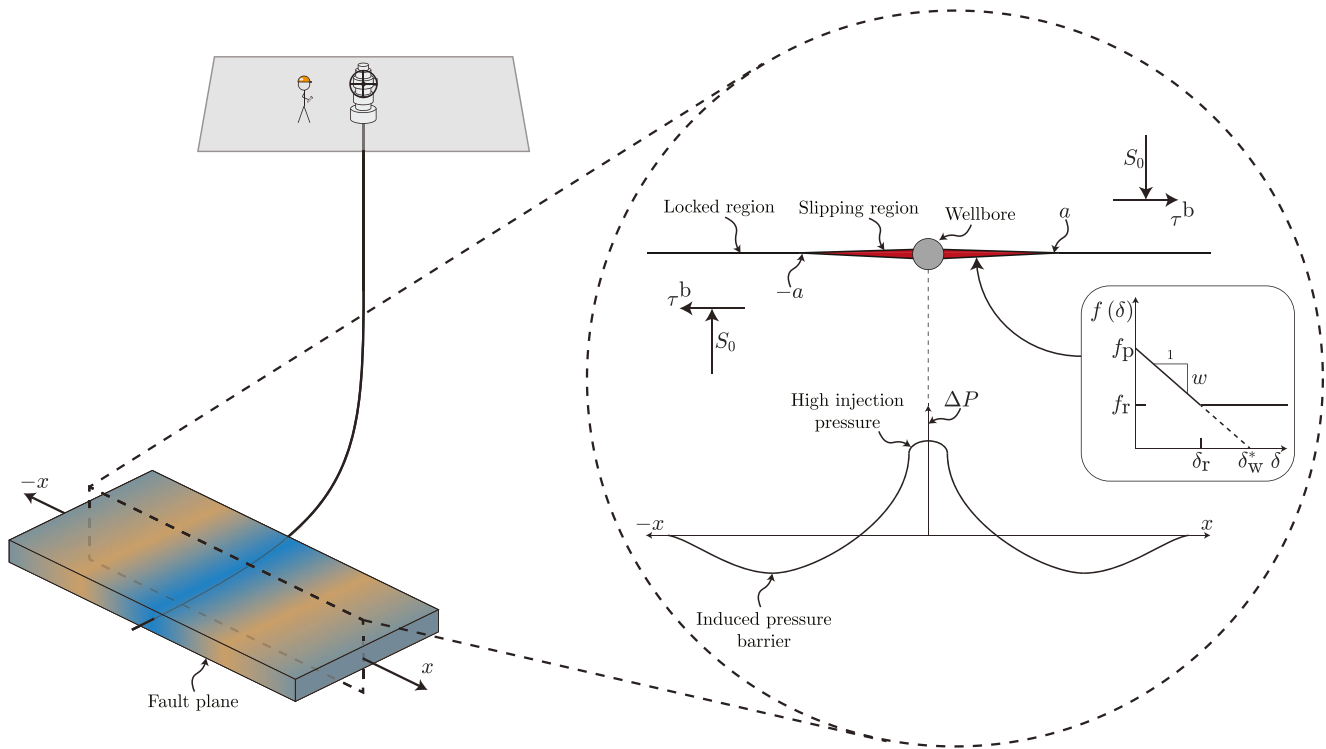


**Figure 1.** Problem overview. A wellhead at the surface connected to a wellbore that intersects a target fault in a parallel fashion. The fault is stimulated after pore pressure preconditioning. The specific geometry of this setup allows for a 1-D investigation. (*Lens, above*) A schematic of a 1-D fault with a total normal stress,  $S_0$ , and background shear stress,  $\tau^b$ , acting on it. The crack tip is located at  $\pm a$ . Beyond the crack tip the fault is locked. Closer to the wellbore the fault is slipping. (*Lens, below*) An example change in pore pressure profile along the fault when preconditioning is employed. The change in pore pressure,  $\Delta P$ , is large and positive near the wellbore where injection is occurring, but negative far from the wellbore due to previous production (preconditioning). (*Lens, inset*) A representation of the linear slip-weakening law used to relate friction,  $f(\delta)$ , to slip,  $\delta$ . The peak friction,  $f_p$ , residual friction,  $f_r$ , linear slip-weakening coefficient,  $w$ , slip required to achieve residual friction,  $\delta_r$ , and characteristic slip,  $\delta_w^*$  are also represented.

Sibson, 1985). By extending the original model of Garagash and Germanovich (2012) to include piece-wise fluid injection and production, the combination of a 1-D analytical flow model coupled to an earthquake nucleation and propagation model will be used to show how the proposed stimulation strategy is able to shift the nucleation behavior of a stimulated fault thereby reducing the risk of a runaway seismic event when compared to the base case of simple fluid injection.

## 2. Methodology

The specific case of a well intersecting the plane of a fault is considered here (Figure 1). This allows the problem to be modeled in 1-D. The well is assumed to maintain constant down-hole pressures, and leak-off along the fault is neglected; meaning an analytical solution for pore pressure evolution can be used. The behavior of the fault is then modeled with a linear slip-weakening formulation. This combined model is based on Garagash and Germanovich (2012).

### 2.1. Governing Equations

#### 2.1.1. Analytical Fluid Model

Beginning with the conservation of mass balance and considering a constant fluid viscosity and constant and isotropic permeability, the pressure diffusion equation can be written as,

$$\frac{\partial P}{\partial t} - D \nabla^2 P = q, \quad (1)$$

where  $P$  is the pore fluid pressure,  $t$  is time,  $q$  is the source term, and  $D = \frac{k}{\eta\phi c_t}$  is the diffusivity, where  $k$  is the permeability,  $\eta$  is the fluid dynamic viscosity,  $\phi$  is the porosity, and  $c_t$  is the total compressibility. Being of the same form as the heat equation, analytical solutions are well known.

The analytical solution to Equation 1 for a constant wellbore injection pressure in 1-D can be written as (Carslaw & Jaeger, 1959; Garagash & Germanovich, 2012),

$$P(x, t) = P_0 + \Delta P_i \operatorname{Erfc} \left| \frac{x}{\sqrt{Dt}} \right|, \quad (2)$$

where  $P_0$  is the initial pore pressure,  $x$  the location,  $\Delta P_i$  the injection pressure used for stimulation, and  $\operatorname{Erfc}$  the complementary error function. This model corresponds to a line source in a fault without leakoff. In the case that the wellbore pressure changes in a piece-wise manner, producing and then injecting, the analytical solution can be written as,

$$P(x, t) - P_0 = \begin{cases} \Delta P_p \operatorname{Erfc} \left| \frac{x}{\sqrt{D(t+t_p)}} \right| & -t_p < t \leq 0 \\ \Delta P_p \operatorname{Erfc} \left| \frac{x}{\sqrt{D(t+t_p)}} \right| + (\Delta P_i - \Delta P_p) \operatorname{Erfc} \left| \frac{x}{\sqrt{Dt}} \right| & t > 0, \end{cases} \quad (3)$$

where  $\Delta P_p$  is the difference between pre-injection production pressure and  $P_0$  and is by definition negative. Further,  $t_p$  is the time used for pre-injection production. From this point onward,  $t = 0$  will correspond to the onset of injection.

### 2.1.2. Earthquake Model

Following the model of Garagash and Germanovich (2012), a 1-D symmetrical shear crack of length  $2a$  is assumed to be located in a uniform background stress field, with a constant normal total stress,  $S_0$ , and background shear stress,  $\tau^b$ , acting on it. The definition of the normal total stress further yields the definition of Terzaghi's effective normal stress,  $\sigma = S_0 - P$ . Through quasi-static elastic equilibrium, the shear stress,  $\tau$ , is related to the slip,  $\delta$  (Bilby & Eshelby, 1968; Garagash & Germanovich, 2012),

$$\tau(x, t) - \tau^b = -\frac{\mu^*}{2\pi} \int_{-a}^a \frac{\partial \delta(s, t)}{\partial s} \frac{ds}{x-s}. \quad (4)$$

Here,  $\mu^*$  is equivalent to the shear modulus,  $\mu$ , for mode III and  $\frac{\mu}{1-\nu}$  for mode II, where  $\nu$  is Poisson's ratio. Two constraints are imposed on the distribution of  $\tau$  along the crack, which result from a finite slip rate at the crack tips (Garagash & Germanovich, 2012; Rice, 1968a),

$$\int_{-a}^a \frac{\tau(x, t) - \tau^b}{\sqrt{a(t)^2 - x^2}} dx = 0, \quad \int_{-a}^a \frac{\tau(x, t) - \tau^b}{\sqrt{a(t)^2 - x^2}} x dx = 0. \quad (5)$$

These two conditions ensure that the stress intensity factor at the crack tip is balanced by the cohesive frictional forces, leaving no singularity. Due to the symmetry of the shear stress and pore pressure distributions with respect to the borehole location ( $x = 0$ ), crack expansion is symmetric, and the second constraint is automatically satisfied. In the region where slip is occurring, the shear stress is equivalent to the fault strength,

$$\tau = f(\delta)\sigma, \quad (6)$$

where  $f$  is the friction coefficient, which is given by,

$$f(\delta) = \begin{cases} f_p - w\delta & \delta \leq \delta_r \\ f_r & \delta > \delta_r. \end{cases} \quad (7)$$

Here,  $f_p$  is the peak value of friction and  $w$  is the linear slip-weakening coefficient (e.g., Garagash & Germanovich, 2012; Ida, 1972). Note that the slip required to achieve residual friction,  $f_r$ , is denoted by  $\delta_r = \frac{f_p - f_r}{w}$ , whereas the slip and crack length at the nucleation of a dynamic event are denoted, where applicable, by  $\delta_{nuc}$  and  $a_{nuc}$ , respectively. This model leads to the definition of a characteristic length scale,  $a_w^* = \frac{\mu^* \delta_w^*}{f_p \sigma_0^*}$ , based on a characteristic slip,  $\delta_w^* = \frac{f_p}{w}$ , and a characteristic effective stress,  $\sigma_0^* = S_0 - P_0$ .

Equations 4, 6, and 7 are then used to evaluate the quasi-static behavior of a slipping crack due to a change in fault strength caused by a change in pore pressure (Garagash & Germanovich, 2012; Uenishi & Rice, 2003), where slip is activated when,

$$\tau^b \geq \tau^p - f_p(P - P_0), \quad (8)$$

with  $\tau^p = f_p \sigma$  representing the peak shear stress the fault can support. A schematic of the model setup is shown in Figure 1, and tables summarizing the variables used are presented in Appendix A.

Note that this linear slip-weakening model represents a simplification of natural faults, which generally exhibit more complicated weakening (e.g., Pagliarunga et al., 2022) and as well as frictional healing (Dieterich, 1972). Further, the analysis here concerns a constant-permeability 1-D fault without leak-off under quasi-static equilibrium. These assumptions are addressed in Section 4.5.

### 2.1.3. Small Scale Yielding Model

In the case that the quasi-static crack length is large compared to a characteristic length,  $a_w^*$ , slip weakening is localized in a small zone near the crack tip, and the small scale yielding (s.s.y.) approach is implemented (Garagash & Germanovich, 2012; Palmer & Rice, 1973; Rice, 1968a, 1968b). Then, the fracture energy,  $G_c$ , is evaluated as,

$$G_c \simeq (f_p - f_r) \sigma(a) \frac{\delta_r}{2}, \quad (9)$$

by assuming that the effective normal stress is approximately constant near the crack tip and has a value of  $\sigma(a)$ . The mode-II stress intensity factor,  $K$ , considering the far-field stress and the residual fault strength, is written as the sum of the contributions of the total stress drop and the local changes in pore pressure associated with fluid injection,

$$K = (\tau^b - \tau^r) \sqrt{\pi a} + \Delta K(a, t), \quad (10)$$

where,

$$\Delta K(a, t) = f_r \sqrt{\frac{a}{\pi}} \int_{-a}^a \frac{P(x, t) - P_0}{\sqrt{a^2 - x^2}} dx, \quad (11)$$

and the residual shear stress  $\tau^r = f_r \sigma$ . Note that the residual shear stress is the strength of the fully weakened fault. At the initiation of slip, shear stress is reduced down to a minimum value corresponding to the residual shear stress. Residual shear stress is dependent on the effective normal stress and therefore by extension also the pore pressure. The rate at which elastic energy can be quasi-statically released in the crack tip region due to crack propagation can then be evaluated as  $G = \frac{K^2}{2\mu^*}$ . The condition for stable crack propagation,

$$\frac{K^2}{2\mu^*} = G_c, \quad (12)$$

then yields the asymptotic solution for the crack length. In this work, the s.s.y. approach is used for crack lengths larger than  $7a_w^*$ . More details on this model can be found in Garagash and Germanovich (2012).

### 2.2. Scaling

The problem is generalized by introducing a number of dimensionless quantities and expressing the relevant variables as the product of a characteristic quantity and a dimensionless variable. The characteristic quantities

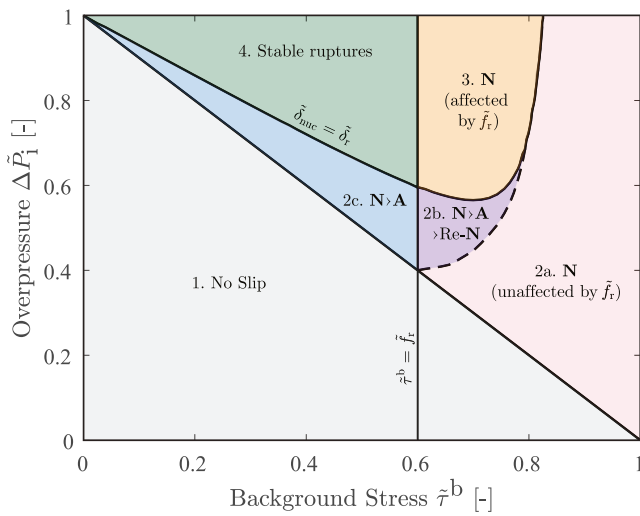


**Figure 2.** Nucleation regime overview. An overview of the nucleation regimes presented by Garagash and Germanovich (2012) in their figure 11 and adapted for presentation here. Results pertain to a given overpressure during injection,  $\Delta\bar{P}_i$ , at a given background stress, or stress criticality,  $\bar{\tau}^b$ , with no preconditioning. This results in a number of characteristic nucleation behaviors, or regimes. These nucleation regimes are designated by a number: 1, 2a, 2b, 2c, 3, or 4, with **N** referring to the nucleation of a dynamic event, and **A** referring to its arrest. In regime 1 slip is not initiated as  $\Delta\bar{P}_i < 1 - \bar{\tau}^b$ . Regimes 2c and 4 result in ultimately stable sliding as  $\bar{\tau}^b < \bar{f}_r$ . Regimes 2a, 2b, and 3 result in an un-arrested dynamic event as  $\bar{\tau}^b > \bar{f}_r$ . In the case of regime 2b, an initial dynamic event is arrested before a second, runaway dynamic event nucleates. Regime 3 is affected by  $\bar{f}_r$  as the slip at nucleation is large enough to allow the fault to reach residual friction (i.e.,  $\bar{\delta}_{nuc} > \bar{\delta}_r$ ). Note that the curve  $\bar{\delta}_{nuc} = \bar{\delta}_r$  is found numerically; see Garagash and Germanovich (2012), figure 8e.

are time-independent. The characteristic length scales are denoted by the previously defined characteristic slip  $\delta_w^*$  and length  $a_w^*$ . The characteristic effective stress,  $\sigma_0^*$ , has also been previously defined. Finally, the characteristic time is given by  $t^* = \frac{a_w^{*2}}{D}$ . The introduction of these characteristic quantities allows for the definition of the following dimensionless variables, introduced for convenience,

$$\begin{aligned}\tilde{x} &= \frac{x}{a_w^*}, & \tilde{a} &= \frac{a}{a_w^*}, & \tilde{a}_{nuc} &= \frac{a_{nuc}}{a_w^*}, & \tilde{t} &= \sqrt{\frac{t}{t^*}}, & \tilde{t}_p &= \sqrt{\frac{t_p}{t^*}}, \\ \Delta\tilde{P} &= \frac{P - P_0}{\sigma_0^*}, & \Delta\tilde{P}_p &= \frac{\Delta P_p}{\sigma_0^*}, & \Delta\tilde{P}_i &= \frac{\Delta P_i}{\sigma_0^*}, \\ \tilde{f}_r &= \frac{f_r}{f_p}, & \tilde{\tau} &= \frac{\tau}{\tau^p}, & \tilde{\tau}^b &= \frac{\tau^b}{f_p \sigma_0^*}, \\ \tilde{\delta} &= \frac{\delta}{\delta_w^*}, & \tilde{\delta}_{nuc} &= \frac{\delta_{nuc}}{\delta_w^*}, & \tilde{\delta}_r &= \frac{\delta_r}{\delta_w^*}, \\ \tilde{G}_c &= \frac{2G_c \mu^*}{f_p^2 (S_0 - P_0)^2 a_w^*}, & \tilde{K} &= \frac{K}{f_p (S_0 - P_0) \sqrt{a_w^*}}.\end{aligned}\quad (13)$$

As previously introduced by Garagash and Germanovich (2012), this approach leads to a number of characteristic behaviors, restated here for clarity (Figure 2).

### 3. Results

The general principle of pore pressure preconditioning is that, by reducing the pressure along the fault far from the well, ruptures that nucleate in the near-wellbore region, where the pore pressure is high during injection, will either be suppressed or propagate into the low-pressure region and be arrested. This would allow for the stimulation of the near-wellbore region with a reduced risk of a runaway rupture. Ultimately of course, as injection continues, the previously created pressure barrier will be undone as pore pressure rises. At this stage runaway rupture would still occur. Relevant points of

understanding for pore pressure preconditioning are therefore related to the creation of a pressure barrier, this barrier's ability to alter the nucleation behavior of an eventual early-time earthquake, and its influence on the ultimate late-time runaway rupture. These topics will therefore form the core of this results section.

#### 3.1. The Creation of a Pressure Barrier

When a period of pre-production is followed by injection, a pressure barrier is formed which steadily moves away from the injection well and reduces in magnitude. This pressure barrier can be characterized by the minimum value of the pressure profile and this minimum's location. Its location,  $\tilde{x}_b$ , moves away from the well in time and can be found by  $\frac{\partial \Delta\tilde{P}(\tilde{x}, \tilde{t})}{\partial \tilde{x}} = 0$ , such that, in 1-D for fixed production and injection pressures,

$$\tilde{x}_b(\tilde{t}) = \xi \tilde{t} \sqrt{\tilde{t}^2 + \tilde{t}_p^2}, \quad (14)$$

where,

$$\xi = \frac{1}{\tilde{t}_p} \sqrt{\ln \left( \left( 1 - \frac{\Delta\tilde{P}_i}{\Delta\tilde{P}_p} \right) \sqrt{1 + \frac{\tilde{t}_p^2}{\tilde{t}^2}} \right)}. \quad (15)$$

The value of the pressure minimum reduces in magnitude with time and is given by,

$$\Delta\tilde{P}(\tilde{x}_b, \tilde{t}) = \Delta\tilde{P}_p \text{Erfc}[\xi \tilde{t}] + (\Delta\tilde{P}_i - \Delta\tilde{P}_p) \text{Erfc} \left[ \xi \sqrt{\tilde{t}^2 + \tilde{t}_p^2} \right]. \quad (16)$$



Considering that the scaled fracture energy can be given by,

$$\tilde{G}_c = \frac{2G_c\mu^*}{f_p^2(\sigma_0^* - P_0)^2 a_w^*} \simeq (1 - \tilde{f}_r)^2 (1 - \Delta\tilde{P})^2, \quad (17)$$

the fracture energy barrier scales with the square of the pressure barrier. That the fracture energy barrier scales with the pore pressure barrier is consistent with the notion that fracture energy is the energy dissipated per unit of nominal contact area and that the real contact area increases with the normal load (Bayart et al., 2018). The significance of the barrier depends on the durations and magnitudes of both the production and injection phases. While not addressed here, similar pressure barriers can be created in both 2-D and 3-D and also for constant-rate wells.

### 3.2. Spatially Delaying Dynamic Rupture

#### 3.2.1. Demonstration of Rupture Delay

For certain combinations of injection pressure and background stress, preconditioning will delay the nucleation of a runaway dynamic rupture, Figure 3. Nucleation in instances of high background stress and no preconditioning are characterized by regime 2a. This situation corresponds to a *critically stressed* fault, which is more likely to host dynamic events (Garagash & Germanovich, 2012). In this regime, the crack length at nucleation can be predicted by  $\tilde{a}_{\text{nuc}} = \frac{0.579}{\tilde{\tau}^b}$  (Garagash & Germanovich, 2012). In this sense, the crack length at nucleation for these cases does not depend on the injection pressure and is solely controlled by the initial weakening behavior of the frictional interface. However, by performing preconditioning before injection, the nucleation regime can be changed to regime 3. In regime 3, this analytical expression no longer holds and the crack length at nucleation is larger than the analytically predicted value for regime 2a. If production has changed the nucleation regime from 2a to 3, nucleation also only occurs once the crack length has extended beyond the pore pressure minimum. This suggests that pore pressure preconditioning has potential to drive a fault away from criticality.

As an example, a case is shown where  $\tilde{f}_r = 0.6$ ,  $\tilde{\tau}_b = 0.95$ , and  $\Delta\tilde{P}_i = 0.7$  (Figure 3). A comparison is made between no preconditioning and a preconditioning characterized by  $\Delta\tilde{P}_p = -0.5$  and  $\tilde{t}_p = 10$ . As predicted by the analytical expression, the case of no preconditioning has a nucleation length of 0.625, occurring after an injection time of 0.06. The preconditioned case, however, is driven away from criticality and does not follow the analytical prediction, having a nucleation length of 1.81, occurring after an injection time of 0.75. Further, at the moment where both cracks have achieved a crack length corresponding to the analytically predicted nucleation length, the preconditioned case has achieved significantly more slip along the crack (Figure 3c), at a lower slip velocity (Figure 3d). It is further propagating in a region of higher fracture energy which is less critically stressed (Figures 3e and 3f). That the fault in this region is less critically stressed implies that the stress drop available to fuel the propagation of the crack tip is also reduced. Further, it can be seen in Figure 3f that the center of the crack has reached residual friction and is therefore sliding in a slip-neutral manner.

#### 3.2.2. The Effect of Production Time and Magnitude

The duration of the production phase and its magnitude both have a significant influence on the effect of the preconditioning phase. Larger production times and magnitudes lead to larger and more significantly preconditioned zones. This results in not only temporally delayed nucleation but also in nucleation lengths that are larger than those in the case that the reservoir is not preconditioned.

For example, in Figures 4a, 4c, and 4e, an example is shown where  $\tilde{f}_r = 0.6$ ,  $\tilde{\tau}^b = 0.8$ ,  $\Delta\tilde{P}_i = 0.8$ , and  $\tilde{t}_p = 100$ , but  $\Delta\tilde{P}_p$  is varied, assuming the values  $-0.3$ ,  $-0.5$ , and  $-0.7$ . Injection is continued until  $\tilde{t} = 10$ . Compared to the case of no preconditioning where the nucleation length is 0.8 occurring after an injection time of 0.29, the cases where  $\Delta\tilde{P}_p$  is equal to  $-0.3$  and  $-0.5$  have nucleation lengths of 9.15 and 30.80 occurring after injection times of 2.00 and 8.91, respectively. The case where  $\Delta\tilde{P}_p = -0.7$  has not yet nucleated a dynamic event after an injection time of 10, and instead has quasi-statically grown a crack of length 14.60. Of course, once the injection period is no longer small when compared to the production period, the pore pressure changes incurred by preconditioning will have been largely undone and the nucleation of a dynamic event will follow.

Similarly, Figures 4b, 4d, and 4f show an example where  $\tilde{f}_r = 0.6$ ,  $\tilde{\tau}^b = 0.8$ ,  $\tilde{P}_i = 0.8$ , and  $\Delta\tilde{P}_p = -0.5$ , but  $\tilde{t}_p$  is varied, assuming the values 3, 30, and 300. Injection is continued until  $\tilde{t} = 10$ . Compared to the case of no

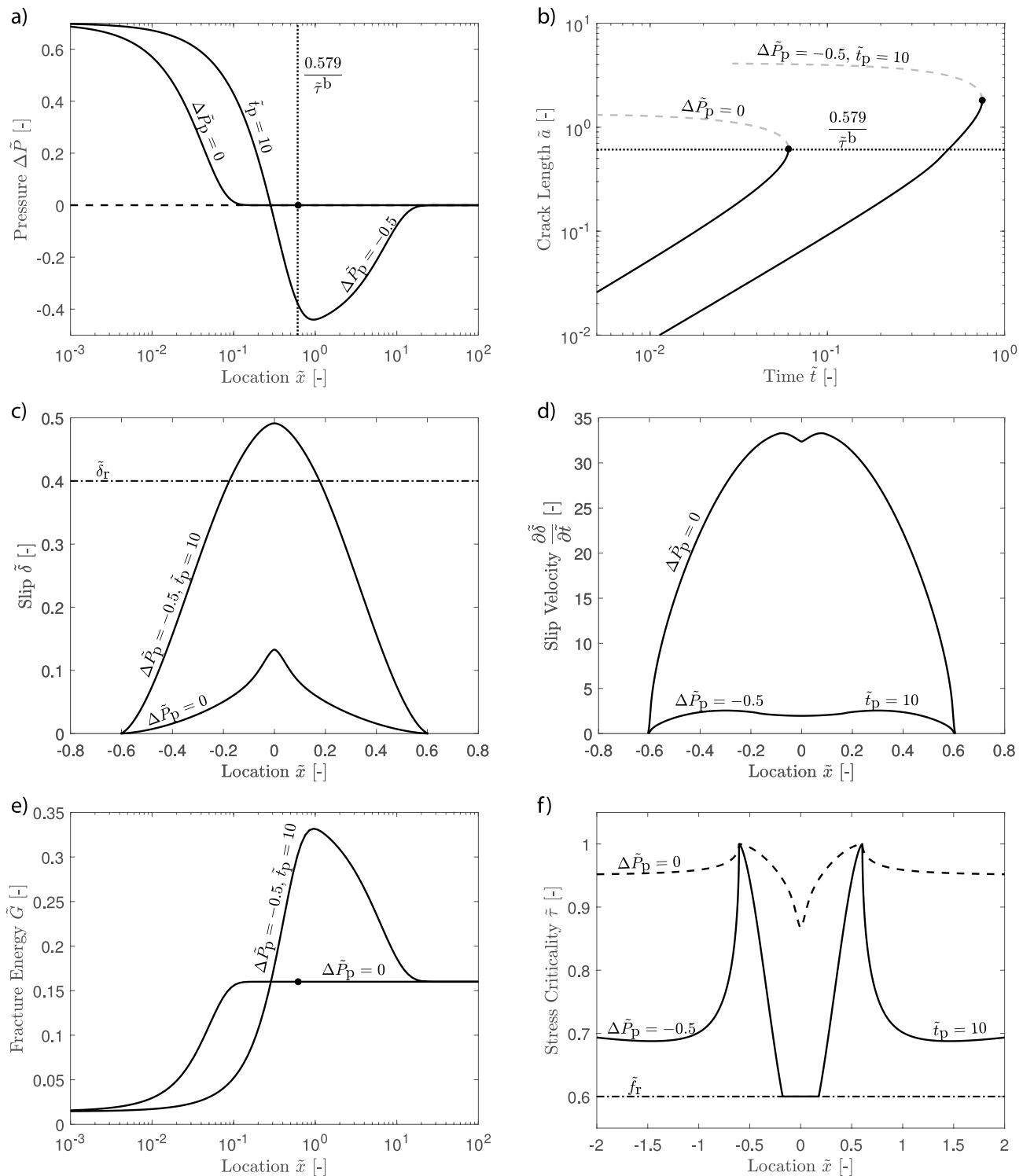


Figure 3.

preconditioning where the nucleation length is 0.8 occurring after an injection time of 0.29, the case where  $\tilde{t}_p$  is equal to 3 and 30 have nucleation lengths of 2.03 and 10.68 occurring after injection times of 1.01 and 3.90, respectively. The case where  $\tilde{t}_p = 300$  has not yet nucleated a dynamic event after an injection time of 10, and instead has quasi-statically grown a crack of length 20.49.



### 3.3. Halting Dynamic Rupture

#### 3.3.1. Demonstration of Rupture Halting

To demonstrate pore pressure preconditioning's ability to arrest a rupture that would otherwise have led to a runaway event, an example case is compared to the base case of no pre-injection production (Figure 5). In both cases,  $\tilde{f}_r = 0.6$ ,  $\tilde{\tau}^b = 0.8$ , and  $\Delta\tilde{P}_1 = 0.4$ . In the case of preconditioning,  $\Delta\tilde{P}_p = -0.5$  and  $\tilde{t}_p = 10$ . In both instances, a dynamic event was nucleated after achieving a crack length of 0.75. The required injection time to achieve this nucleation was 0.58 when no preconditioning was employed and 1.41 when there was preconditioning. In the case of no preconditioning, this nucleation led to a runaway event, whereas with preconditioning this event was arrested at a crack length of 0.89. It then continued to grow stably until a time of 2.74 and a crack length of 4.83 before re-nucleating, this time leading to uncontained dynamic rupture. The slip profiles in Figures 5c and 5d show that the preconditioned case achieved larger values of slip at lower slip velocities at the nucleation of the first event. This dynamic event then propagated into a zone that was less critically stressed (Figure 5f), and was characterized by a larger fracture energy (Figure 5e). Preconditioning can arrest a propagating dynamic rupture in this manner because it creates a fracture energy barrier (Figure 5e), and slows down the crack by reducing the energy available at the crack tip through a decrease in the available stress drop (Figure 5f), even resulting in values of  $\tilde{\tau}$  which are less than  $\tilde{f}_r$ ; both of these elements can be seen to play a major role, for example, in the s.s.y. propagation criterion (Equation 12).

In this example, the nucleation behavior was altered from runaway dynamic event nucleation, regime 2a, to contained dynamic event nucleation and arrest followed by dynamic event nucleation, regime 2b. Further, the slipping patch length at nucleation of a runaway dynamic event was increased by a factor of 6.4.

#### 3.3.2. The Influence of Background Stress

The effect of preconditioning is also dependent on the background stress and injection pressure, similar to the original regimes of Garagash and Germanovich (2012). To illustrate the influence of background stress, two cases are presented, each comprised of five background stresses. In the first case,  $\Delta\tilde{P}_p = -0.3$ , whereas in the second case  $\Delta\tilde{P}_p = -0.7$ . In both cases  $\tilde{f}_r = 0.6$ ,  $\Delta\tilde{P}_1 = 0.3$ , and  $\tilde{t}_p = 3$ . The background stresses are 0.75, 0.8, 0.85, 0.9, and 0.95. In the first case, Figures 6a and 6c, the preconditioning is insufficient to alter the nucleation regime, and the nucleation length is given by the analytical solution of Garagash and Germanovich (2012). However, in the second case, Figures 6b and 6d, the first dynamic event is nucleated and then arrested by the pressure barrier for all but the lowest values of background stress. The crack then propagates quasi-statically until passing the pressure barrier and re-nucleating a dynamic event. Therefore, not only does sufficient preconditioning lead to the arrest of an otherwise runaway event, the runaway event which ultimately occurs only nucleates when the crack length has grown beyond the pressure minimum induced by the preconditioning. As operators will be able to exhibit a fair amount of control over the location of the pressure minimum and are capable of taking down-hole pressure measurements, this opens up the possibility to a degree of operator control over the nucleation of the runaway dynamic event.

### 3.4. Nucleation Regime Change

Preconditioning's ability to alter the nucleation regime is a reflection of its ability to delay or halt dynamic events before runaway. For this reason, the change in nucleation regime across the entire space of possible injection pressures and background stresses is a relevant tool for the assessment of the efficacy of the preconditioning. To achieve the delay or arrest of a dynamic rupture that would have otherwise been a runaway event, a certain level of pre-injection production is required, depending on both the magnitude and duration of the production.

**Figure 3.** An illustration of preconditioning's ability to delay the nucleation of dynamic rupture on a critically stressed fault, for  $\tilde{f}_r = 0.6$ ,  $\tilde{\tau}_b = 0.95$ , and  $\Delta\tilde{P}_1 = 0.7$ . Two cases are shown, one case without pre-injection production and one where  $\Delta\tilde{P}_p = -0.5$  and  $\tilde{t}_p = 10$ . (a) The pore pressure profiles at the moment when both cracks have achieved the analytical nucleation length, given by  $\frac{0.579}{\tilde{\tau}^b}$  (Garagash & Germanovich, 2012). The crack length at nucleation for the case without preconditioning is given by the black dot; the preconditioned case has not yet nucleated a dynamic event. The analytically predicted nucleation length for regime 2a is shown by the vertical dotted line. Regime 3's nucleation length is always larger than this analytically predicted value. The key point is therefore that preconditioning has changed the nucleation regime from 2a to 3 and delayed nucleation. (b) The development of crack length in time. Faded dotted lines represent non-physical solutions. The (c) slip, (d) slip velocity, (e) fracture energy, and (f) stress criticality at the analytically predicted nucleation length. Note that the preconditioned case has not yet nucleated a dynamic event at this point. In (c), the slip required to reach residual friction is given by a dashed-dotted line. In (f), the residual friction is denoted by a dashed-dotted line.

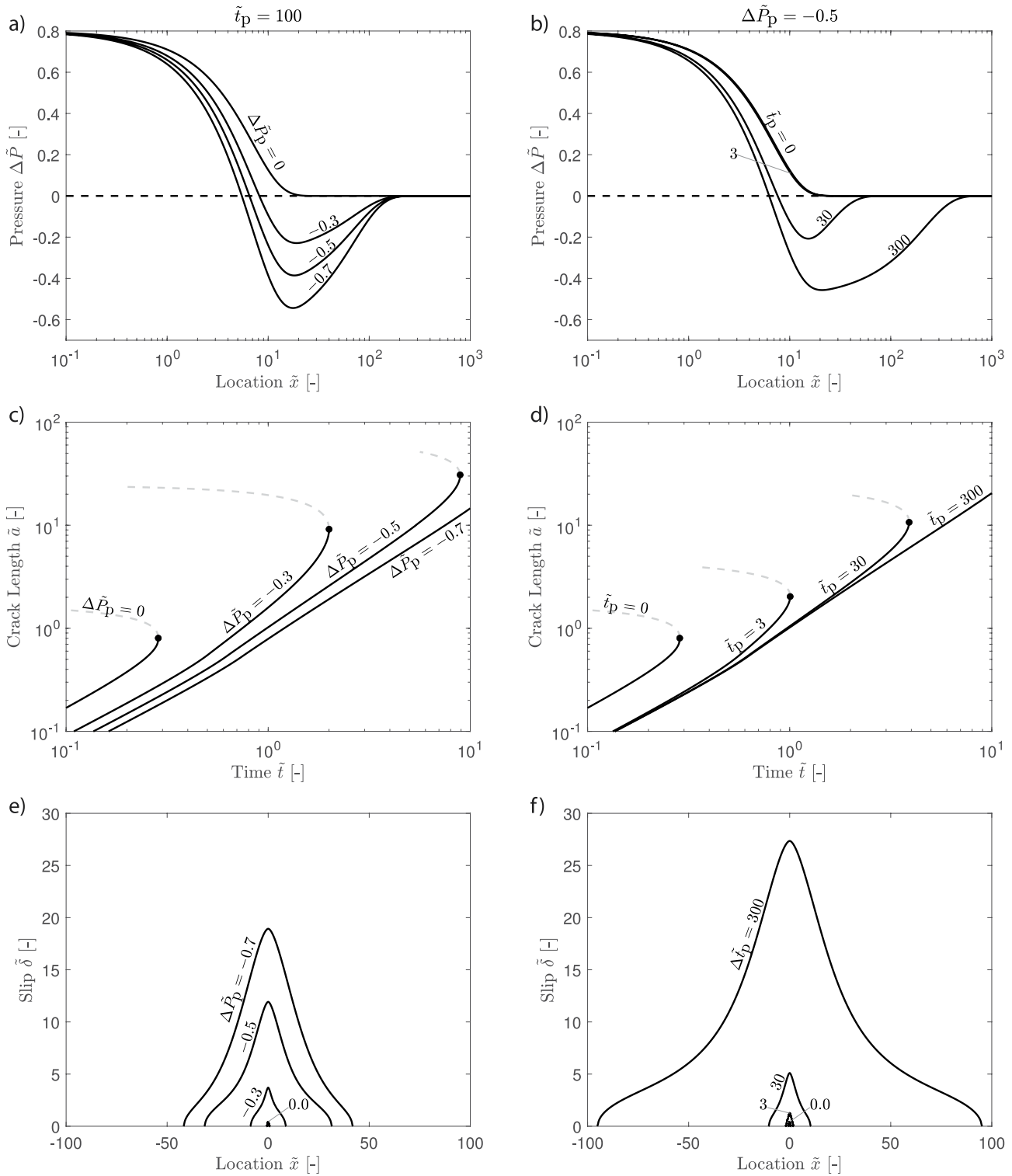


Figure 4.

A further dependence on the injection pressure, background stress, and residual friction will also be present, as demonstrated for the case of no preconditioning by Garagash and Germanovich (2012). Figure 7 illustrates the influence of the magnitude of the production phase for one production duration across the space of possible injection pressures and background stresses.

As the production time is increased, larger regions of the reservoir are preconditioned. This results in higher values of background stress having their nucleation lengths significantly increased, with the slipping zone's size before nucleation of a runaway dynamic event reaching a size orders of magnitude larger than it would have been able to without preconditioning (Figure 8).

### 3.5. Long Production, Short Injection Asymptotic

#### 3.5.1. Required Production Magnitude

Long production phases essentially alter the background stress in the entire region seen by the rupturing crack during nucleation. When the crack length due to injection is large compared to  $a_w^*$ , but has still not left the preconditioned zone, the s.s.y. approach can be used to evaluate the stress intensity factor (Garagash & Germanovich, 2012),

$$\tilde{K} = \sqrt{\pi \tilde{a}} (\tilde{\tau}^b - \tilde{f}_r) + \tilde{f}_r \sqrt{\frac{\tilde{a}}{\pi}} \int_{-\tilde{a}}^{\tilde{a}} \frac{\Delta \tilde{P}(\tilde{x}, \tilde{t})}{\sqrt{\tilde{a}^2 - \tilde{x}^2}} d\tilde{x}, \quad (18)$$

with the crack propagation criterion written as,

$$\tilde{K}^2 = \tilde{G}_c. \quad (19)$$

Assuming that injection is occurring in a fully preconditioned reservoir, such that the pore pressure was homogeneous before injection, and that the crack has run far ahead of the zone of pore pressure increase caused by fluid injection, Equation 18 can be rewritten as,

$$\tilde{K} = (\tilde{\tau}_b - \tilde{f}_r) \sqrt{\pi \tilde{a}} + \Delta \tilde{P} \tilde{f}_r \sqrt{\pi \tilde{a}}, \quad (20)$$

implying that the contribution of the initial background stress to the stress intensity factor is canceled out by the reduction in pore pressure when,

$$\Delta \tilde{P} \leq 1 - \frac{\tilde{\tau}^b}{\tilde{f}_r}. \quad (21)$$

This criterion is equivalent to saying that the stress criticality must become less than the residual friction,  $\tilde{\tau} < \tilde{f}_r$ , as found by Garagash and Germanovich (2012) and shown experimentally by Cebry et al. (2022). In this case, the crack will still be able to propagate due to the increase of pore pressure near the wellbore, but, like for the criterion derived by Garagash and Germanovich (2012), the crack will be ultimately stable as long as it remains in the preconditioned zone.

While it has been possible to provide a criterion for the required magnitude of production, the amount of production time required to effectuate a regime change in nucleation is difficult to constrain. It essentially corresponds to the amount of production required such that, when injection commences, the region near the injection well will fully weaken before the nucleation of a dynamic event, and, therefore,  $\tilde{t}_p$  must be significantly larger than one, considering that time is normalized by  $a_w^*$ .

#### 3.5.2. Re-Scaling

When significant fluid production has been achieved, the dimensionless background stress and dimensionless injection pressure can be re-scaled, based on their original definitions, to consider the preconditioned pore pressure field as  $\tilde{\tau} = \frac{\tilde{\tau}^b}{1 - \Delta \tilde{P}_p}$  and  $\frac{\Delta \tilde{P}_i - \Delta \tilde{P}_p}{1 - \Delta \tilde{P}_p}$ . Using this updated scaling, the results of three cases where the  $\tilde{t}_p \gg 1$  are plotted,

**Figure 4.** A demonstration of how increasing (a, c, e) the magnitude of production,  $\Delta \tilde{P}_p$ , and (b, d, f) the duration of production,  $\tilde{t}_p$ , during preconditioning can result in larger stress barriers and delay nucleation, resulting in more slip across a wider area (and therefore a larger stimulated zone) before the nucleation of a runaway dynamic event. (a, b) Pore-pressure-profile versus distance-from-wellbore example cases for an injection pressure  $\Delta \tilde{P}_i = 0.8$  and injection time  $\tilde{t} = 10$ , with the initial pressure denoted by the dashed line. (a) The pre-injection production time is set to  $\tilde{t}_p = 100$  and the magnitude of the production  $\Delta \tilde{P}_p$  assumes the values 0,  $-0.3$ ,  $-0.5$ , and  $-0.7$ . Note that  $\Delta \tilde{P}_p = 0$  corresponds to the base case of no pre-injection production. (b) The pre-injection production magnitude is set to  $\Delta \tilde{P}_p = -0.5$  and the time of the production  $\tilde{t}_p$  assumes the values 0, 3, 30, and 300. Note that  $\tilde{t}_p = 0$  corresponds to the base case of no pre-injection production and that both (a) and (b) are independent of background stress. (c, d) show the development of the crack for both of these cases when  $\tilde{f}_r = 0.6$  and  $\tilde{\tau}^b = 0.8$ , with the black dot corresponding to the nucleation of a runaway dynamic event. Faded dotted lines represent non-physical solutions. (e, f) show the slip profiles at the eventual moment of nucleation.

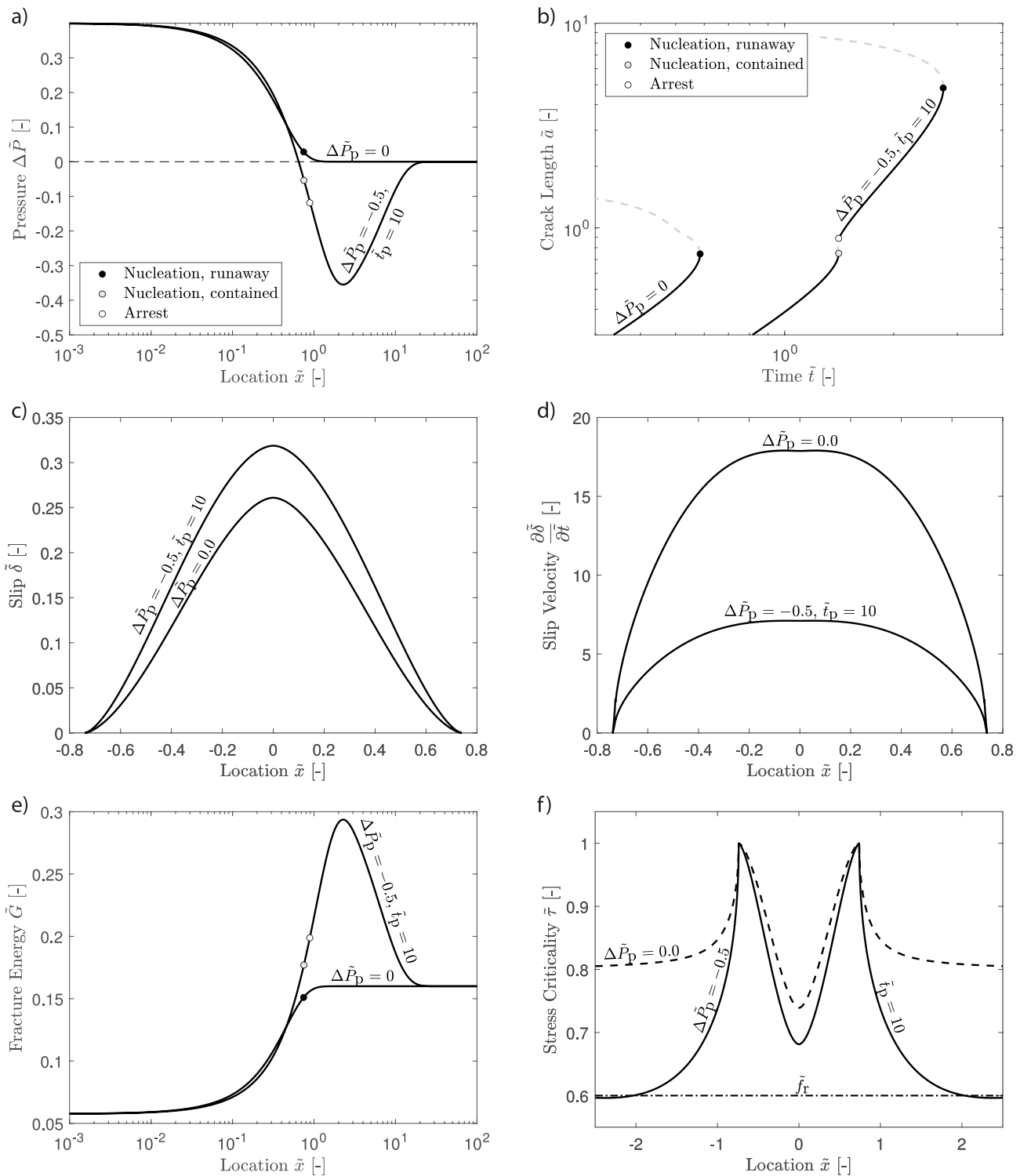


**Figure 5.** An example comparison demonstrating rupture halting between the base case of no pre-injection production and a preconditioned case where, for both cases,  $\tilde{f}_r = 0.6$ ,  $\tilde{\tau}^b = 0.8$ , and  $\Delta \tilde{P}_i = 0.4$ . For the case that preconditioning is employed,  $\Delta \tilde{P}_p = -0.5$  and  $\tilde{t}_p = 10$ . (a) The pore pressure profiles at the time of the nucleation of the first dynamic event. In the case of no preconditioning this nucleation leads to a runaway event, whereas it leads to arrest for the preconditioned case. (b) The development of crack length with injection time for both cases. Faded dotted lines represent non-physical solutions. (c)–(f) The slip, slip velocity, fracture energy, and stress criticality profiles at the moment of nucleation of the first dynamic event. In (a, b, e), the crack tip location at nucleation of a runaway dynamic event is given by a black dot, at nucleation of a contained event by a gray dot, and at arrest by a white dot. In (f), the residual friction is denoted by a gray dot.

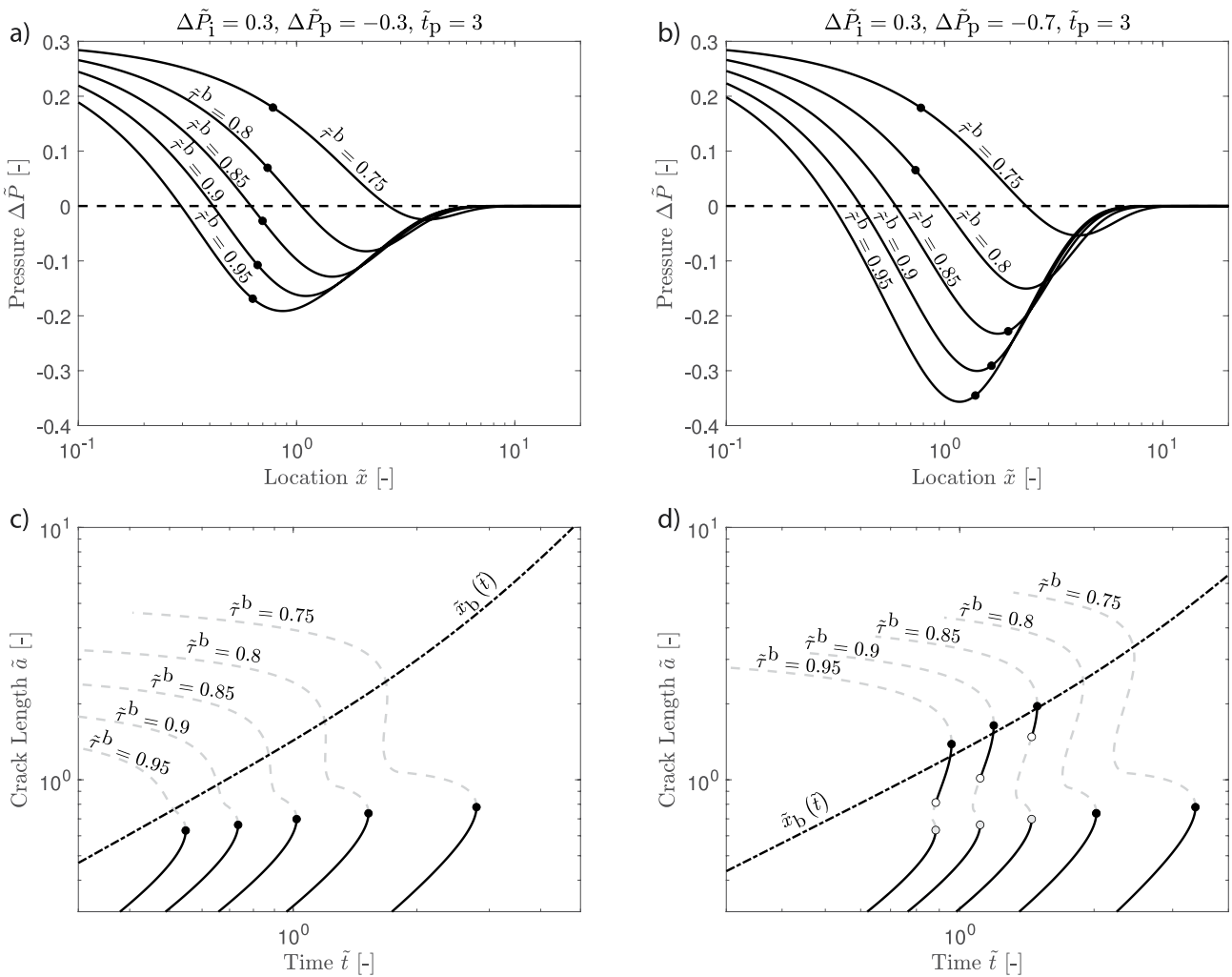


**Figure 6.** A demonstration of how applying a larger magnitude of production,  $\Delta\tilde{P}_p$ , can lead to arrested rupture for a variety of background stresses,  $\tilde{\tau}^b$ . (a, c) The case where pre-injection production lasted for  $\tilde{t}_p = 3$  with a magnitude of  $\Delta\tilde{P}_p = -0.3$  before injection at  $\Delta\tilde{P}_1 = 0.3$  occurred. (a) The pore pressure profiles at nucleation of a runaway event for different values of  $\tilde{\tau}^b$ . The length of the crack at the nucleation of a runaway dynamic event is denoted by the black dot. (c) The development of crack length versus time for these same values of  $\tilde{\tau}^b$ . Runaway ruptures are denoted by black dots. The position of the minimum value of pore pressure is shown by the dark dashed-dotted line. Faded dotted lines represent non-physical solutions. (b, d) The same plots for the case where pre-injection production had a magnitude of  $\Delta\tilde{P}_p = -0.7$  (d) Contained ruptures are denoted by gray dots, and the arrest of a rupture is denoted by a white dot. Note the runaway dynamic ruptures occurring after passing the pressure barrier in the case of arrested rupture. In all cases  $\tilde{f}_r = 0.6$ .

up until an arbitrary crack length of  $\tilde{a} = 20$  (Figure 9). This crack length is larger than the nucleation crack lengths for non-preconditioned critically stressed reservoirs. However, it can still be considered early time for these simulations because  $\tilde{t} \ll \tilde{t}_p$  and the behavior is governed by the preconditioned- and not the original-background stress.

Note the similarities between the results plotted with this altered scaling in Figures 9a, 9c, and 9e and the original case with no pre-injection production (Figure 7a). As long as the period of injection is small and  $\frac{\tilde{\tau}^b}{1-\Delta\tilde{P}_p} < \tilde{f}_r$ , the cases which previously led to runaway dynamic rupture will now follow the nucleation behavior of regimes 2c and 4. The allowable injection time such that the assumption of small injection times holds is dependent on the duration and magnitude of production and the initial background stress. Note that if injection were to continue, the stress changes associated with preconditioning would be undone and the runaway dynamic events associated with cases where  $\tilde{\tau}^b > \tilde{f}_r$  would ultimately result. The amount of time required to grow the crack to a length of  $\tilde{a} = 20$  is shown in Figures 9b, 9d, and 9f, such that the crack grows significantly slower in those cases where  $\frac{\tilde{\tau}^b}{1-\Delta\tilde{P}_p} < \tilde{f}_r$ .

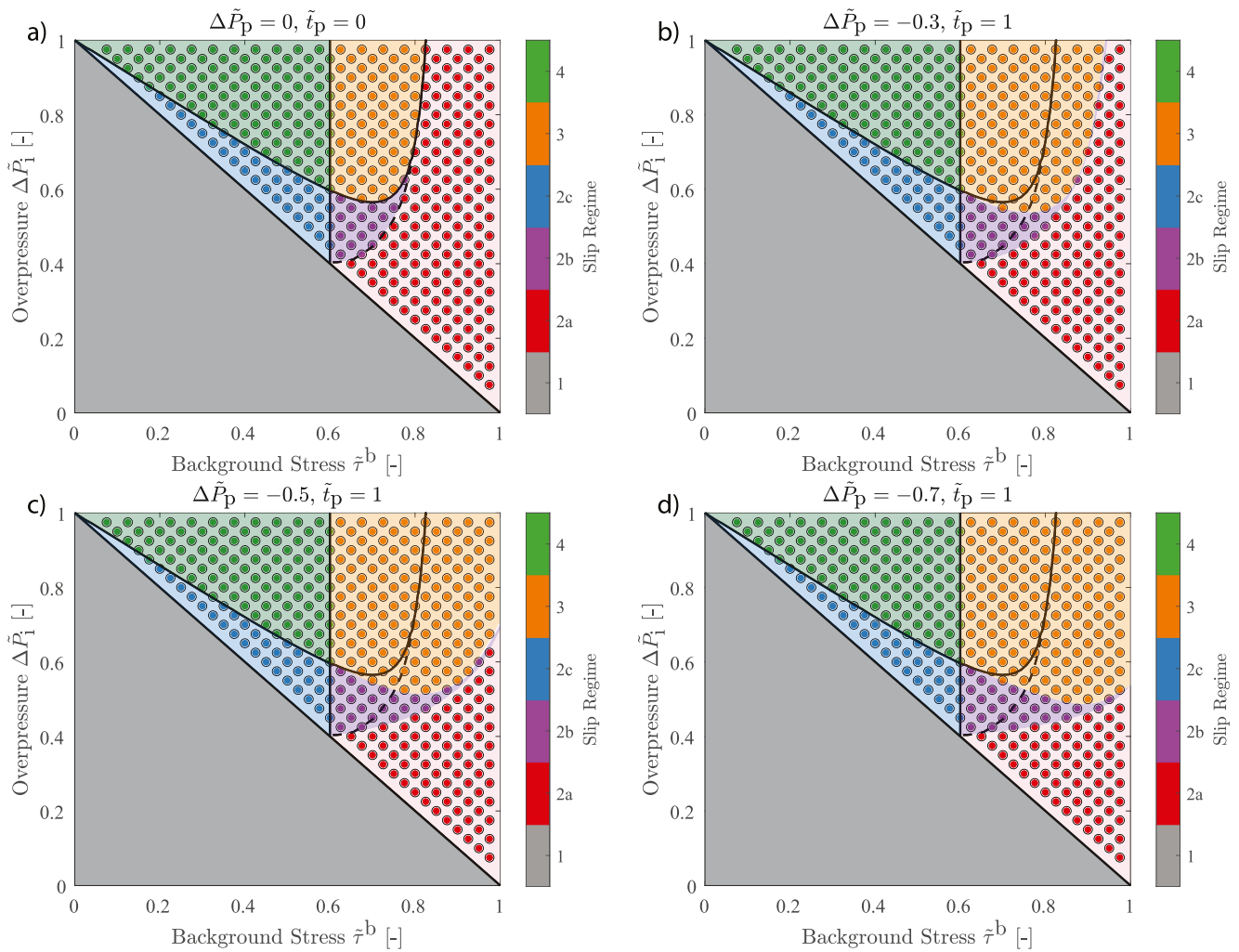


**Figure 7.** The nucleation regime as a function of the overpressure-background stress parameter space for various magnitudes of production,  $\Delta\tilde{P}_p$ . These numerical results can be compared to the base diagram in Figure 2. Each point corresponds to one simulation, with the color denoting its slip regime as defined by Garagash and Germanovich (2012). In regime 1 (gray), the increase in pore pressure is not sufficient to activate slip. Regime 2a (red) corresponds to runaway dynamic slip. Regime 2b (purple) corresponds to nucleation of dynamic slip followed by arrest and then re-nucleation of runaway dynamic slip. Regime 2c (blue) corresponds to nucleation of dynamic slip followed by arrest and ultimate stability. Regimes 2a–2c are not affected by residual friction such that slip at nucleation  $\delta_{nuc}$  is less than  $\delta_r$ . Regime 3 (orange) corresponds to runaway dynamic slip where nucleation is affected by residual friction such that  $\delta_{nuc}$  is larger than  $\delta_r$ . Regime 4 (green) is stable, with no dynamic slip. (a) corresponds to the case of no pre-injection production, an equivalent to Garagash and Germanovich (2012), their figure 11, or Figure 2 here. Production lasting  $\tilde{t}_p = 1$  is displayed for (b)  $\Delta\tilde{P}_p = -0.3$ , (c)  $\Delta\tilde{P}_p = -0.5$ , and (d)  $\Delta\tilde{P}_p = -0.7$ . Note how production is able to change the regime type for ultimately unstable cases. The vertical line corresponds to  $\tilde{f}_r$ . In all cases,  $\tilde{f}_r = 0.6$ . The line separating regimes 2c and 4 corresponds to  $\tilde{\delta}_{nuc} = \tilde{\delta}_r$ . The boundaries between regimes 2a, 2b, and 3 are the same as in Figure 2 for (a), but altered for (b)–(d) and delimited by shading. For comparison, the original boundaries between these regimes are always shown by black lines.

## 4. Discussion

### 4.1. Changing the Nucleation Regime

As can be seen in Figure 7a, there exist background stresses for which dynamic rupture will occur for small nucleation lengths, in particular for near-critically stressed faults. Critically stressed faults are common, not just in general (e.g., Harrison et al., 1954), but especially in EGS applications (Evans et al., 2012). One implication of the work of Garagash and Germanovich (2012), therefore, is that it may be difficult to achieve large shear-stimulated zones in EGS without triggering a runaway dynamic rupture. Indeed, creating a stimulated reservoir while avoiding significant levels of seismicity has proven to be a problem for EGS. However, the results here indicate that pre-stimulation reservoir production can potentially provide a solution. In particular, preconditioning has been shown to result in a regime change, either halting or delaying what would otherwise be a



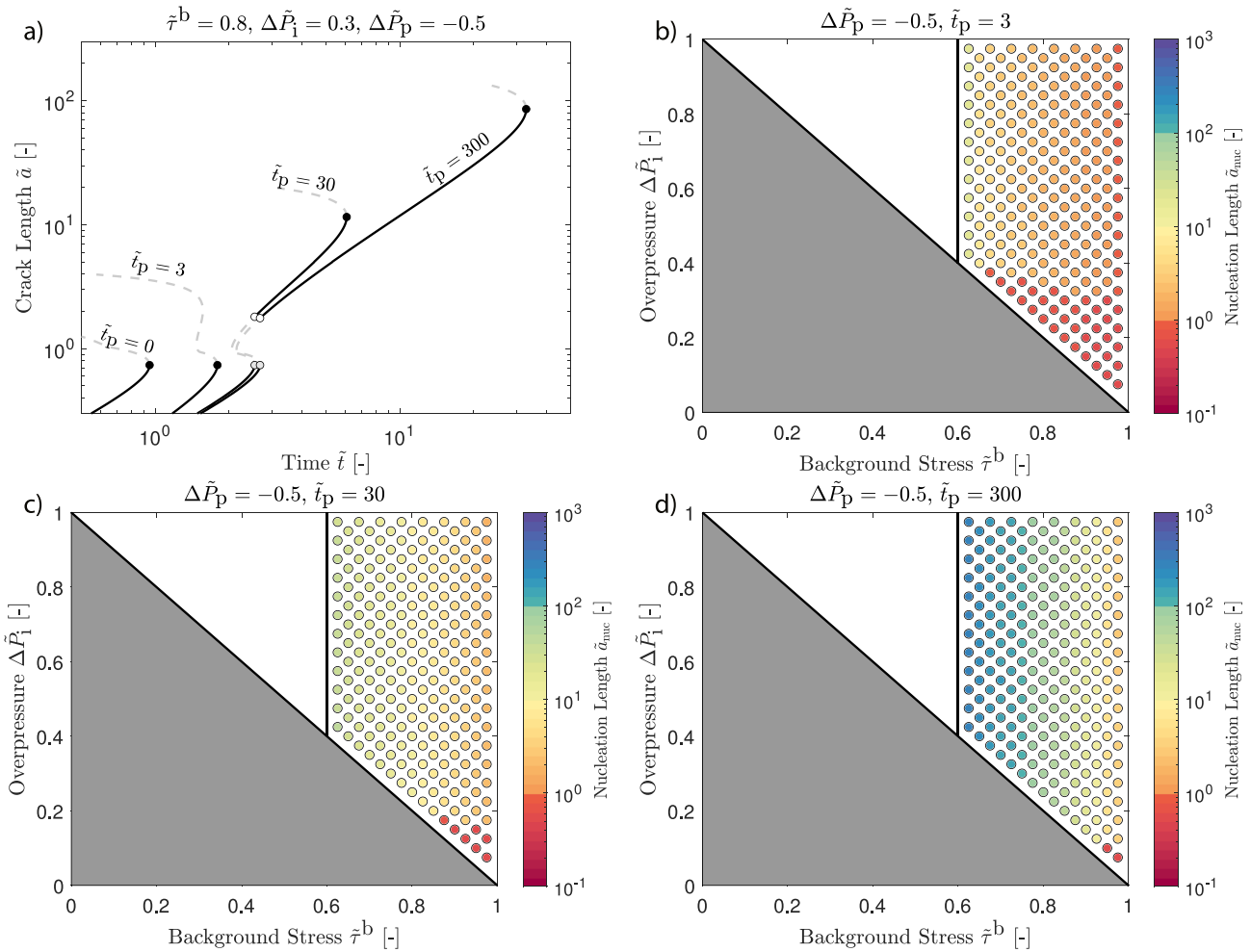


**Figure 8.** A comparison of runaway nucleation for varying values of  $\tilde{t}_p$ , with  $\Delta\tilde{P}_p = -0.5$ . This figure demonstrates how increasing production time,  $\tilde{t}_p$ , increases the ultimate nucleation length of a runaway dynamic event. (a) The crack length development as a function of injection time, for the specific case of  $\tilde{\tau}^b = 0.8$  and  $\Delta\tilde{P}_1 = 0.3$ . Four different production durations are shown, with  $\tilde{t}_p = 0$  corresponding to the base case of no pre-injection production. Black circles correspond to the nucleation of runaway dynamic rupture, gray circles correspond to the nucleation of a foreshock that is ultimately contained, and white circles correspond to the point of arrest. Faded dotted lines represent non-physical solutions. (b)–(d) show, for (b)  $\tilde{t}_p = 3$ , (c)  $\tilde{t}_p = 30$ , and (d)  $\tilde{t}_p = 300$ , the size of the slipping patch at the nucleation of runaway dynamic rupture for a wide variety of background stresses and injection pressures. The vertical line corresponds to  $\tilde{\tau}^b = \tilde{f}_r$ . In all cases,  $\tilde{f}_r = 0.6$ .

runaway dynamic rupture via both a fracture energy barrier and a reduction in the energy available at the crack tip achieved by a decrease in the potential stress drop. Additionally, the larger values of slip achieved near the injection well mean that faults are more likely to reach residual friction when preconditioning has been applied. These areas of residual friction represent patches of aseismic slip which act to stabilize the rupture through a heterogeneous weakening rate with a central slip-neutral zone, resulting in a larger overall nucleation length (Garagash & Germanovich, 2012; Lebihain, Roch, Violay, et al., 2022). Finally, preconditioning has been shown to result in lower slip velocities along the fault. As thermal weakening mechanisms are generally slip rate dependent and often result in enhanced weakening (Di Toro et al., 2010; Niemeijer et al., 2011; Rice, 2006), this reduced slip velocity may further help to prevent large seismic events.

#### 4.1.1. Halting Dynamic Rupture

In the case that  $\delta_{nuc} < \delta_r$  (regimes 2a–2c), the nucleation length of the first dynamic event for this model is controlled only by the background stress, as shown by Garagash and Germanovich (2012). Under certain conditions, preconditioning has the ability to change the nucleation regime from 2a to 2b, implying the halting of this initial rupture. This is reminiscent of the finding by Uenishi and Rice (2003) that nucleation is unaffected by loading, with the ultimate size of the event being controlled by the conditions on the fault as opposed to the

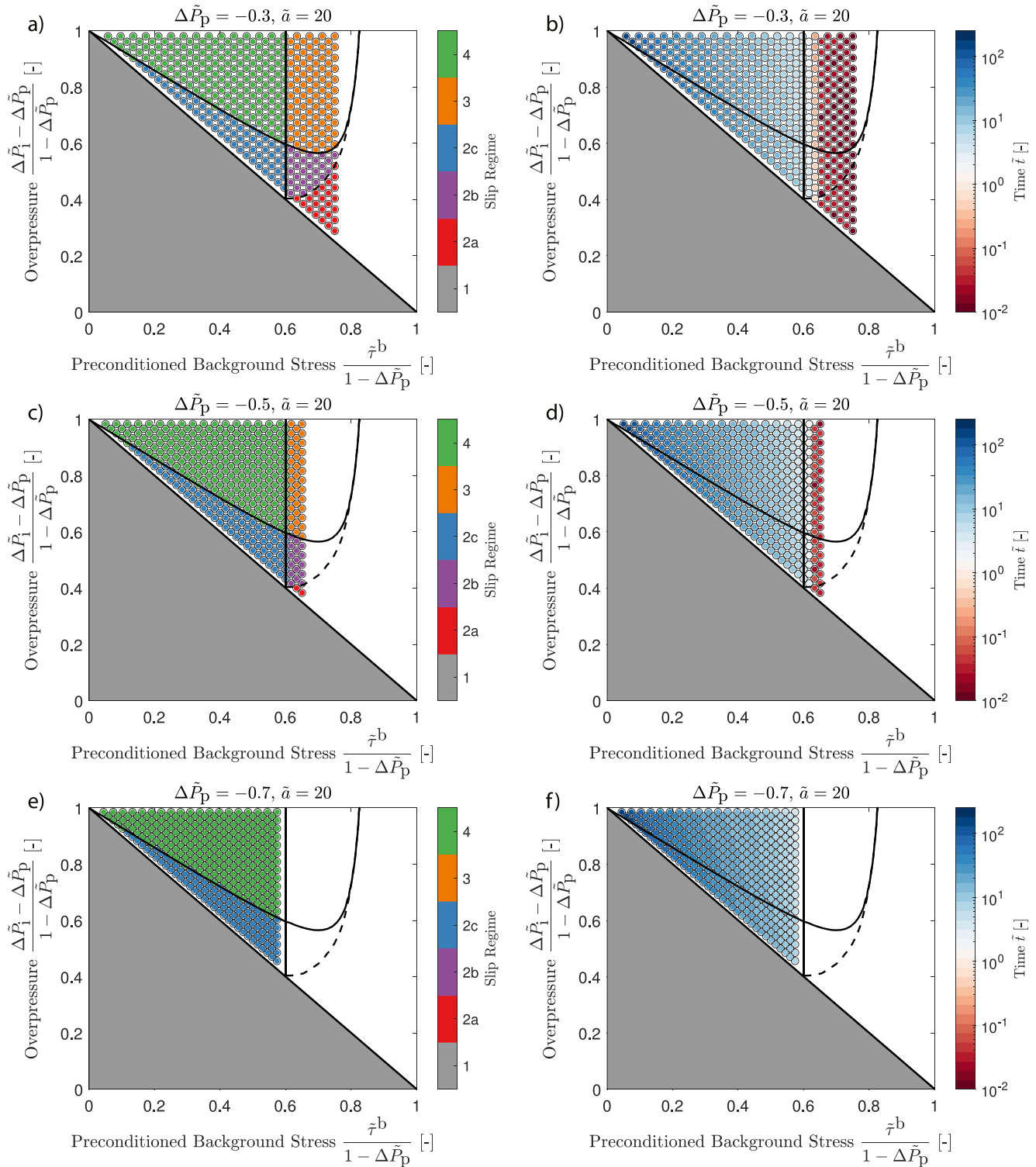


**Figure 9.** The slip regimes as defined by Garagash and Germanovich (2012) and restated here in Figure 2. This figure demonstrates how the scaling developed here captures the behavior of sufficiently preconditioned reservoirs. (a, c, e) These regimes are shown here for a significant duration of production,  $\tilde{t}_p = 300$ , an updated scaling, and a short period of injection, stopping when the crack length  $\tilde{a} = 20$ . (b, d, f) show how long these same cases took to achieve this crack length. (a, b)  $\Delta \tilde{P}_p = -0.3$ , (c, d)  $\Delta \tilde{P}_p = -0.5$ , and (e, f)  $\Delta \tilde{P}_p = -0.7$ . The vertical line corresponds to  $\tilde{f}_r$ . In all cases,  $\tilde{f}_r = 0.6$ . The solid line separating regimes 2c and 4 corresponds to  $\delta_{nuc} = \delta_r$ . The dashed line separates regime 2a from regime 2b in Garagash and Germanovich (2012). The vertical line corresponds to  $\tilde{\tau}^b = \tilde{f}_r$ .

nucleation process (Cebry & McLaskey, 2021; Lapusta et al., 2000). Preconditioning in these cases is not affecting nucleation, but it is altering the conditions on the fault such that the ultimate size of the event is reduced. Preconditioning works by changing the background effective normal stress in the region relevant to the rupturing earthquake. As the shear stress is assumed to be unaffected by the change in pore pressure, an increase in effective normal stress means that the residual shear stress is increasing, reducing the stress drop, and therefore energy, available to the rupturing earthquake, an idea consistent with experiments (Cebry et al., 2022). Dynamic crack propagation being largely sensitive to stress drop (Ampuero et al., 2006; Bayart et al., 2018; Cebry et al., 2022; Garagash & Germanovich, 2012; Ke et al., 2018; Viesca & Rice, 2012), this effect has the ability to halt these ruptures by reducing the amount of energy flowing to the crack tip. Indeed, it has previously been shown numerically that fault sections that were once prone to large seismic ruptures may tend to later halt rupture propagation after a change in stress (Lapusta et al., 2000). Additionally, through an induced increase in effective normal stress, preconditioning results in an increased fracture energy, which acts as a further local barrier to rupture propagation and has been previously shown to be capable of halting a propagating rupture (Bayart et al., 2016, 2018; Gvirtsman & Fineberg, 2021; Hussein et al., 1975). Preventing a dynamic rupture from growing large by halting it with unfavorable conditions along the fault has been shown experimentally to prevent it from efficiently radiating energy (Cebry et al., 2022; Wu & McLaskey, 2018).

#### 4.1.2. Delaying Nucleation

Alternatively, preconditioning can suppress an early time event, delaying its nucleation to a later time, such that the nucleation regime shifts from 2a to 3. This corresponds to preconditioning resulting in a transient shift of the effective background stress such that stable sliding occurs without the nucleation of a dynamic event. Crucially, only when the crack length surpasses the pore pressure barrier imposed by the preconditioning does the nucleation of a dynamic event occur. This transient change in slip mode due to pore pressure changes such that one fault can produce different slip behaviors depending on the injection strategy has been supported by laboratory studies (Passelègue et al., 2020). By selecting the pre-production rate and magnitude, as well as the injection pressure, operators have a certain degree of control over where the pore pressure barrier will be located and what its magnitude will be at any given time.

The significance of either delaying or halting the nucleation of a runaway dynamic event is that once the nucleation regime has been changed from 2a to 2b or 3, the crack is fully weakened near the injection point at the moment of the runaway event and the slip-weakening is localized to a small zone near the crack tip. This zone near the crack tip is characterized by an increasing fracture energy in the region the crack tip propagates into. Therefore, the nucleation of the runaway dynamic event only occurs after the crack tip passes the pore pressure barrier (Figure 10).

### 4.2. Foreshocks

#### 4.2.1. Foreshock Size

Even with preconditioning, foreshocks still occur, appearing now as arrested ruptures in regime 2b. If these foreshocks are significant enough in size, the preconditioning will not be satisfactory despite preventing early time runaway dynamic ruptures from occurring. To assess the magnitude of the foreshocks, a proxy for seismic moment magnitude,  $M_0$ , is used and made dimensionless,  $\tilde{M}_0$ . This dimensionless seismic moment proxy is given by the normalized slip occurring during the foreshock,  $\tilde{\delta}_f = \frac{\delta_f}{\delta_w^*}$ , multiplied by the square of the normalized crack length at arrest,  $\tilde{a}_a = \frac{a_a}{a_w^*}$ ,

$$\tilde{M}_0 = \frac{M_0}{\mu^* \delta_w^* a_w^{*2}} = \tilde{\delta}_f \tilde{a}_a^2, \quad (22)$$

based on the definition of seismic moment (Aki & Richards, 2009). These values are then compared for the most extreme cases of preconditioning tested, where  $\tilde{\tau}_p \gg 1$  (Figure 11). The foreshocks occurring for the cases of preconditioning are generally larger than those for the case without preconditioning, with the largest foreshock occurring without preconditioning having a value of 48.8 and the largest foreshock with preconditioning having a value of 138.3. Note, however, that the simulations which produce the largest foreshocks with preconditioning would be runaway dynamic ruptures in the case of no preconditioning. These values come from scaling and

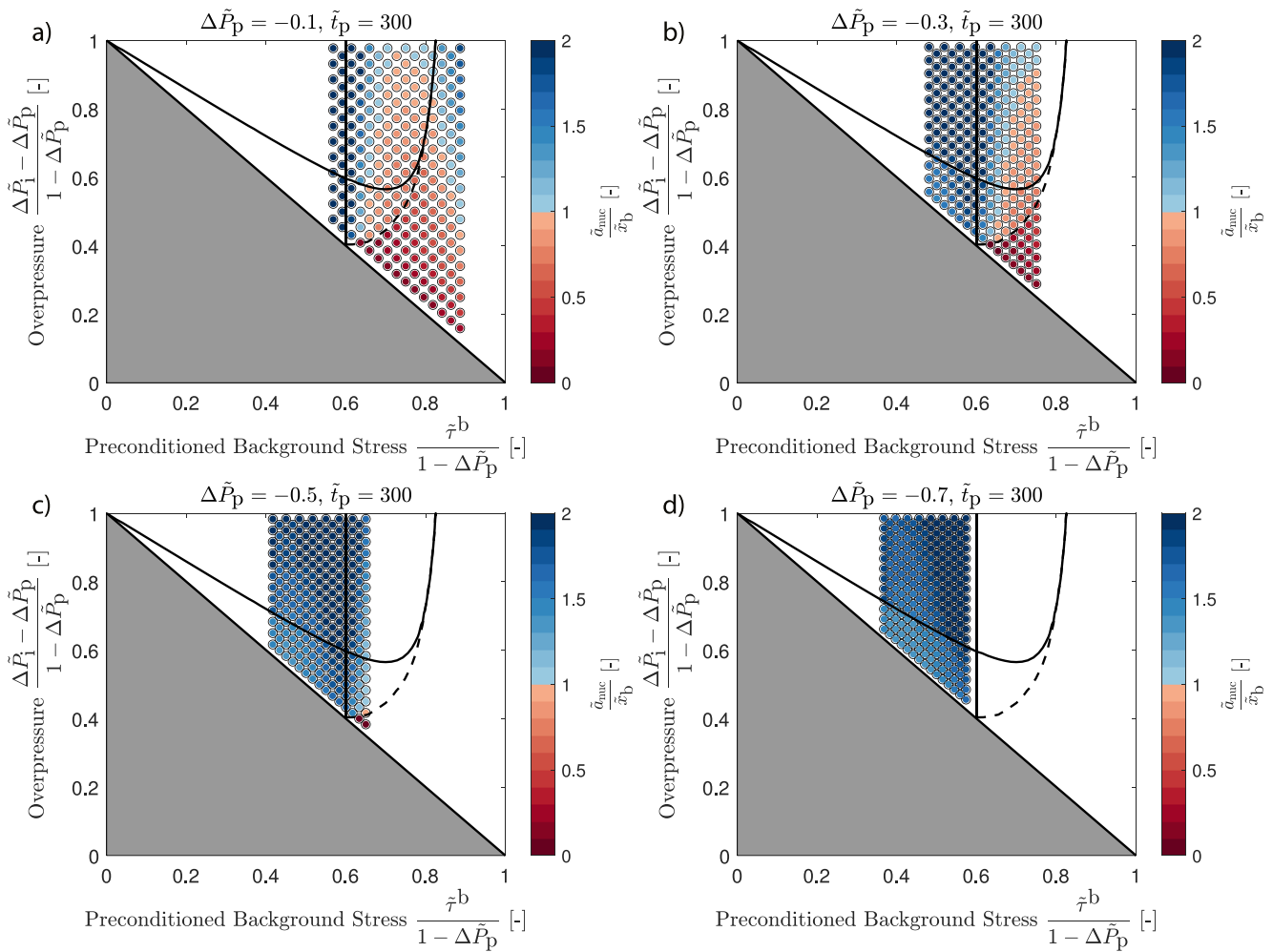


**Figure 10.** An illustration that a sufficient production duration and magnitude lead to the nucleation length of a runaway dynamic event,  $\tilde{a}_{nuc}$ , being farther from the wellbore than the position pressure barrier,  $\tilde{x}_b$ . As illustrated in Figure 9, the magnitude of the pressure production,  $\Delta\tilde{P}_p$  must be such that  $\frac{\tilde{a}_{nuc}}{1-\Delta\tilde{P}_p} < \tilde{f}_r$  (a)  $\Delta\tilde{P}_p = -0.1$ , (b)  $\Delta\tilde{P}_p = -0.3$ , (c)  $\Delta\tilde{P}_p = -0.5$ , and (d)  $\Delta\tilde{P}_p = -0.7$ . The vertical line corresponds to  $\tilde{f}_r$ . In all cases,  $\tilde{f}_r = 0.6$  and  $\tilde{t}_p = 300$ .

are useful for a relative comparison between two cases; however, they can not be converted to actual seismic moments without parameters related to a particular case.

#### 4.2.2. Analytical Prediction of Foreshock Nucleation Length

The analytical solution developed by Garagash and Germanovich (2012) can be used to predict the nucleation lengths of the runaway dynamic ruptures in regime 2a and the foreshocks in regimes 2b and 2c. This analytical solution does not depend on the effective normal stress and the initiation of these events is therefore unaffected by preconditioning as long as the nucleation regime is one of either 2a, 2b, or 2c. However, in the case of preconditioning, these events are arrested, Figure 12. The cases where the nucleation regime moves from 2a to 3 can no longer be represented by this solution as shown previously.

### 4.3. Toward Field Application of Preconditioning

#### 4.3.1. Relevant Field Example

Long-term fluid production from a fault, followed by injection, has not often been tested in the field. However, the German Deep Drilling Site (Shapiro et al., 2006) does offer a relevant example. Here, a fluid extraction experiment was performed for approximately 1 year, producing 22,300 m<sup>3</sup> of saline crustal fluid. This was followed by a 10-month period of injection, which began 1 year after the halting of this production, where 84,600 m<sup>3</sup> of water

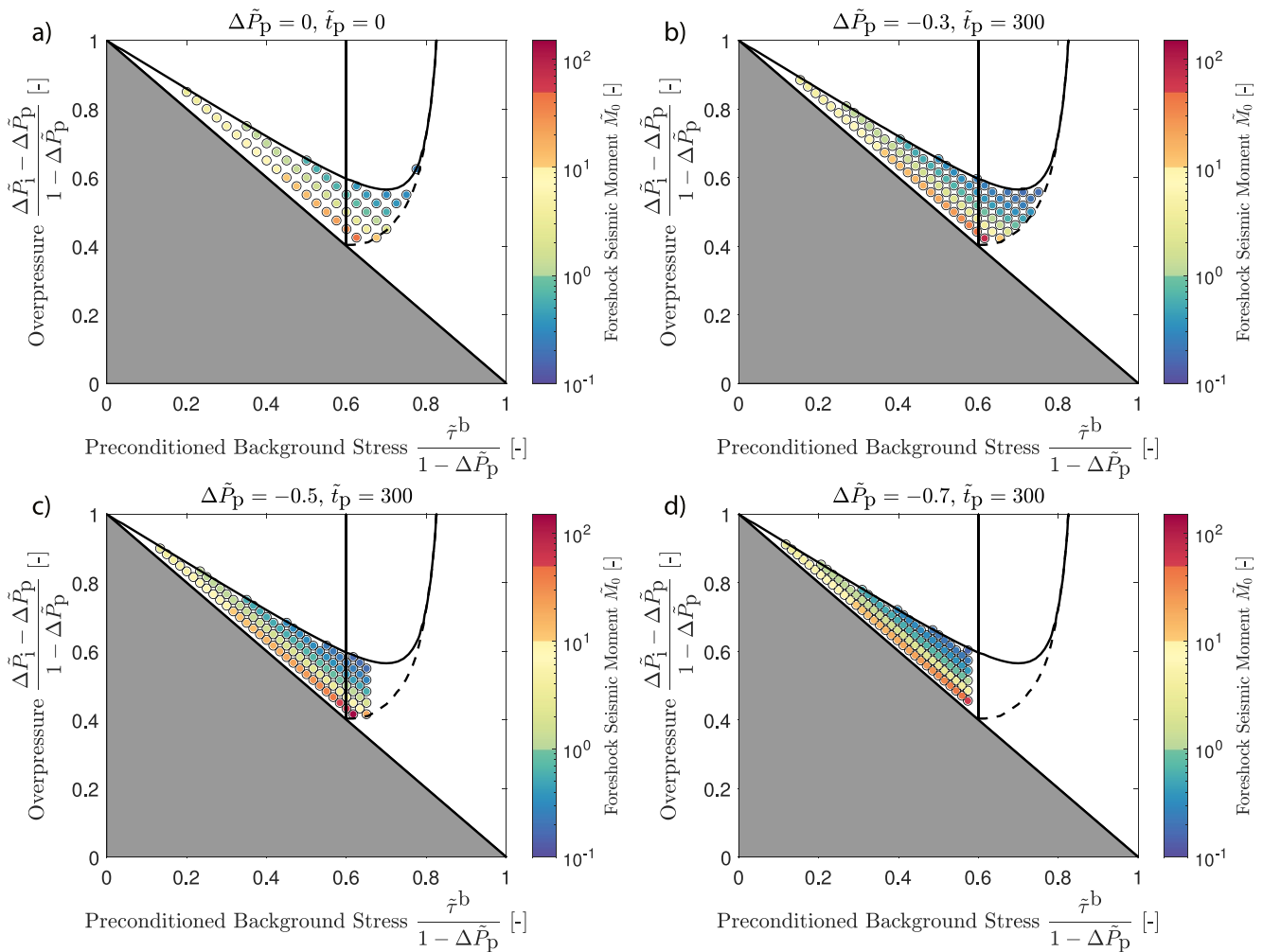


**Figure 11.** A comparison of the foreshock sizes for (a) no pre-injection production, (b)  $\Delta \tilde{P}_p = -0.3$ , (c)  $\Delta \tilde{P}_p = -0.5$ , and (d)  $\Delta \tilde{P}_p = -0.7$ . In (b)–(d),  $\tilde{t}_p = 300$ . The slip multiplied by the square of the crack length at arrest is used as a proxy for foreshock seismic moment, meaning that these are scaling values useful for relative comparison only. The vertical line corresponds to  $\tilde{f}_r$ . In all cases,  $\tilde{f}_r = 0.6$ . The upper-bound line of the simulations plotted corresponds to  $\tilde{\delta}_{nuc} = \tilde{\delta}$ . Note that the last color cutoff begins at  $\tilde{M}_0 = 50$ , which is just above the largest foreshock for the case of no preconditioning, which has a value of 48.8.

was injected. Interestingly, the onset of seismicity in this case approximately corresponded to the time when a net fluid balance (equivalent injected and produced volumes) was achieved. While not a perfect one-to-one example of preconditioning, this field case does provide insight as to its potential application on the field scale. Fluid was produced from a deep ( $\approx 4$  km) fault for a significant period of time, and the injection that began after the halting of this production did not lead to immediate induced seismicity. Admittedly this injection began after a delay which would reduce the pressure barrier's magnitude through diffusion, and should therefore be avoided for effective preconditioning, but for short injection times this procedure still did not result in induced seismicity up until net fluid balance was achieved. Net fluid balance has been seen to be one of the key determining factors directly related to induced seismicity (National Research Council, 2013), such that in cases where more fluid has been removed from the reservoir than injected, as would generally be the case for the preconditioned stimulations introduced here, a reduced number of induced-seismicity-related issues have been encountered.

#### 4.3.2. Required Production Duration and Magnitude

As shown, ensuring late time has been achieved during pre-injection production is related to the idea that the in-situ background stress has been replaced by a background stress with a preconditioned value of pore pressure such that  $\tilde{\tau} < \tilde{f}_r$ , meaning that  $\Delta \tilde{P} \leq 1 - \frac{\tilde{\tau}^b}{\tilde{f}_r}$  must be true for late time to be achieved. This is essentially the same criterion found for dilatancy-induced hardening (Ciardo & Lecampion, 2019) and results in a background stress



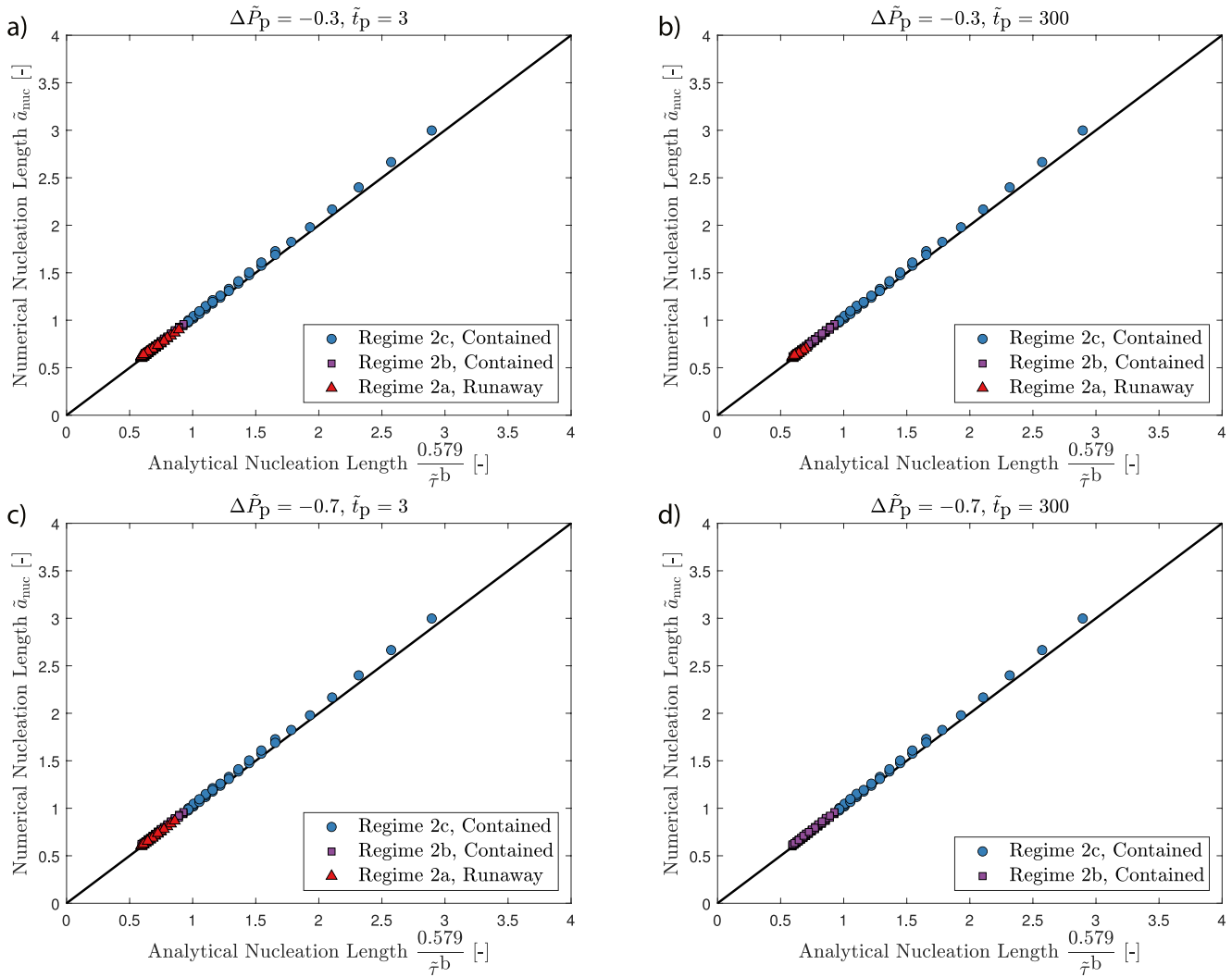


**Figure 12.** A comparison of the crack length of the first nucleated event for regimes 2a–2c given by the simulations and those predicted by the analytical solution of Garagash and Germanovich (2012) for the case of no pre-injection production. Here, pre-injection production is employed, but the scaling still holds as it is only dependent on the value of shear stress, which is independent of normal stress in these simulations. (a)  $\Delta \tilde{P}_p = -0.3$  and  $\tilde{t}_p = 3$ , (b)  $\Delta \tilde{P}_p = -0.3$  and  $\tilde{t}_p = 300$ , (c)  $\Delta \tilde{P}_p = -0.7$  and  $\tilde{t}_p = 3$ , and (d)  $\Delta \tilde{P}_p = -0.7$  and  $\tilde{t}_p = 300$ . Note how the increasing of  $\Delta \tilde{P}_p$  and  $\tilde{t}_p$  does not prevent these early time dynamic slip events from occurring, but does cause their arrest and containment.

state predicted to produce stable sliding in the homogeneous case (Garagash & Germanovich, 2012). Equation 2 can then be restated considering this criterion,

$$1 - \frac{\tilde{\tau}^b}{\tilde{f}_r} > \Delta \tilde{P}_p \operatorname{erfc} \left( \frac{\tilde{x}}{\tilde{t}_p} \right) \quad (23)$$

and rearranged to solve for the required production duration to ensure these pore pressure conditions have been achieved at a given location,  $\tilde{x}_e$ ,

$$\tilde{t}_p > \frac{\tilde{x}_e}{\operatorname{erf}^{-1} \left( \frac{\Delta \tilde{P}_p - 1 + \frac{\tilde{\tau}^b}{\tilde{f}_r}}{\Delta \tilde{P}_p} \right)}, \quad (24)$$

where erf is the error function. The position  $\tilde{x}_e$  in this case corresponds to the extent of the area targeted for stimulation. While this target location might be another well, in certain cases preconditioning the entire area between two wells may prove too challenging. In these cases, the near wellbore region can still be targeted, this



region being the most crucial for improving productivity and injectivity in radial flow regimes (Dake, 1978). The process can then be repeated in a cyclic manner, gradually extending the reach of the stimulated zone.

Note that for smaller values of  $\Delta\tilde{P}_p$  and larger values of background stress, it is not possible to achieve late time because even ubiquitously reducing the pore pressure by  $\Delta\tilde{P}_p$  would not result in the condition  $\tilde{\tau} < \tilde{f}_r$  being met.

As an example of an implementation of preconditioning, a test case relating to the Basel 1 Geothermal System is used (e.g., Häring et al., 2008). A reservoir located at 5 km depth can be expected to experience an overburden yielding a total stress of approximately 115 MPa, assuming  $23 \frac{\text{MPa}}{\text{km}}$ . If normally pressured, the pore pressure will be approximately 50 MPa. It will be assumed that the effective overburden corresponds to the effective normal stress on the fault, and the targeted optimally oriented fault is close to critically stressed, with  $\tilde{\tau}^b = 0.75$  and  $\tilde{f}_r = 0.6$ . Using Equation 21, the required pore pressure change to reduce  $\tilde{\tau}$  to below  $\tilde{f}_r = 0.6$  can be found to be  $-16.3$  MPa. Assuming a diffusivity along the fault of  $0.025 \frac{\text{m}^2}{\text{sec}}$ , reasonable for both Basel (Goertz-Allmann et al., 2011) and the German Deep Drilling Site (Shapiro et al., 2006), and a pre-injection production phase of 1 year, as performed at the German Deep Drilling Site (Shapiro et al., 2006),  $\tilde{\tau}$  can be reduced to below  $\tilde{f}_r = 0.6$  over 450 m away from the wellbore with a bottom-hole production pressure of 15 MPa. It could be envisioned that this location could correspond to a monitoring well. Examples such as these are also helpful for highlighting that this methodology is more readily applicable in cases where the pore pressure to effective normal stress ratio is high. In these cases, each percent pore pressure reduction corresponds to a larger value of dimensionless  $\Delta\tilde{P}_p$ . A relatively high pore pressure to effective normal stress ratio can be found when the reservoir is over-pressured or when the vertical stress is larger than the normal stress (i.e., in normal- and certain instances of strike-slip-faulting stress regimes). Interestingly, it has previously been suggested that the increased normal stress associated with compressive faulting regimes inhibits the ability of small-scale heterogeneities to arrest rupture and lead to foreshocks (Abercrombie & Mori, 1996).

Once sufficient preconditioning has been achieved, the operators could begin stimulating the reservoir with fluid injection. As previously mentioned, the nucleation of a dynamic runaway event will now occur after the crack passes the pressure boundary. The pressure boundary is preceded by the front where the pressure stops decreasing and begins increasing, namely where  $\frac{\partial\Delta\tilde{P}}{\partial\tilde{r}} = 0$ , denoted by  $\tilde{x}_f$ . Reminiscent of the case of shut-in (e.g., Johann et al., 2016), the location of this front is given by,

$$\tilde{x}_f(\tilde{t}) = \frac{\tilde{t}}{\tilde{t}_p} \sqrt{(\tilde{t}^2 + \tilde{t}_p^2) \ln \left( \left( 1 - \frac{\Delta\tilde{P}_1}{\Delta\tilde{P}_p} \right) \left( 1 + \frac{\tilde{t}_p^2}{\tilde{t}^2} \right)^{\frac{3}{2}} \right)}, \quad (25)$$

and can be further tracked with well-bore pressure measurements in the field. For the current case, injection at a constant pressure preceded by production at a constant pressure, this front always precedes the pressure barrier such that  $\tilde{x}_f > \tilde{x}_b$ . In this way, operators can track the location of the advancing pressure barrier. Then, after ensuring that the pressure at their target well has been reduced such that  $\tilde{\tau} < \tilde{f}_r$ , operators could stimulate the reservoir until  $\tilde{x}_f$  passes the target well.

To continue the example given above, the time taken for this front to reach the location 450-m mark (a suitable location for a monitoring well) from the injection location can be found by first assuming a value for  $\mu^* = 34.2$  GPa based on mode-II and taking a Poisson's ratio of 0.22 and a Young's modulus of 65 MPa, values reasonable for the Basel reservoir (Valley & Evans, 2019). A weakening rate  $w\sigma_0^* = 50 \frac{\text{GPa}}{\text{m}}$  is assumed based on the value found by Uenishi and Rice (2003) for Fichtelgebirge granite specimens. Finally, an injection pressure of 74 MPa is taken based on Häring et al. (2008). The result is that pore pressure will begin increasing at the 450-m mark after 422 hr of injection. At this point, the pore pressure barrier is still in between the injection well and the 450-m mark and still corresponds to an area where  $\tilde{\tau}$  is below  $\tilde{f}_r = 0.6$ . In this example, by using preconditioning, operators have been able to stimulate the reservoir for over 17 days in relative safety. Calculations such as these, while crude, highlight the potential usefulness of preconditioning, which can be further developed with more rigorous tests both in the laboratory and at pilot sites.

#### 4.3.3. Post-Stimulation

As shown, even with significant pre-injection production if the injection phase lasts long enough the effect of preconditioning will be undone and runaway dynamic rupture will occur if the original background stress is

higher than the residual friction. Additionally, with successive dynamic events and slip, heterogeneous stress conditions are likely to be erased (Wu & McLaskey, 2018). Further, stress barriers on natural faults, while capable of stopping rupture, have also been shown to act as points of initiation for subsequent seismic events (King, 1986). For this reason, it will be important to address what to do after a sufficient amount of reservoir has been stimulated. Previous field-data sets and modeling-data sets have indicated that fluid pumping and shut-in may be able to halt slip on a previously activated fault (Larochelle et al., 2021). Additionally, analytical work has shown this kind of approach may be able to stop a propagating rupture (Jacquey & Viesca, 2022; Sáez & Lecampion, 2022). The specific effects of pumping and shut-in on rupture propagation are beyond the scope of this work, however.

#### 4.3.4. Other Forms of Preconditioning

As the crack length propagates faster than the pore pressure front when the targeted fault is critically stressed (Bhattacharya & Viesca, 2019; Cebry et al., 2022; Cebry & McLaskey, 2021; Dublanchet, 2019; Garagash & Germanovich, 2012; Guglielmi et al., 2015; Sáez et al., 2022; Viesca, 2022), it may be a challenge to envision stimulation strategies for critically stressed faults which do not pre-emptively alter the far-field conditions encountered by the propagating rupture front.

Similar results to those presented here may be achievable with a pre-injection period of cooling of the reservoir. Thermo-elastic stress changes occurring due to injection/production from horizontal wells are by nature anisotropic, as are stress changes associated with injection/production into highly directional fluid conduits, such as in faults, fractures, and laterally extensive but vertically confined reservoirs. Cooling-induced preconditioning techniques whereby the criticality of the relevant fault has been reduced due to the reduction of differential stress before stimulation can therefore be envisioned (Fryer et al., 2020), albeit with these being possibly impractical due to the more localized nature of thermo-elastic stress changes. Additionally, other authors have suggested fatigue-related preconditioning techniques (Cornet, 2019), which may create scenarios of relatively low fracture energy near the well, ultimately leading to a fracture energy barrier away from the preconditioned region (e.g., Hussein et al., 1975). However, the details of these types of preconditioning are beyond the scope of this work. Note, additionally, that pore pressure preconditioning differs from cyclic stimulation in that it begins with a period of production, which is generally not included in cyclic stimulation (Hofmann et al., 2018, 2021; Zang et al., 2013; Zimmermann et al., 2010). Preconditioning is also based on the creation of a fracture energy barrier and reduces the energy available to the rupture through the increase of residual shear stress, with neither of these phenomena being present in cyclic stimulation. Further, the production duration is significantly longer than the injection duration, whereas in cyclic stimulation, the low and high injection rates have similar durations. This means preconditioning results in a net-negative fluid balance, whereas cyclic stimulation will always be net positive.

#### 4.4. Implications for Heterogeneous Faults

In Section 4.2.2, sufficient fluid production was shown to break the scaling found by Garagash and Germanovich (2012), which predicts the nucleation length of a homogeneous crack. Essentially, producing fluid creates a heterogeneous stress state and barrier around the area of the nucleating event. In terms of natural faults, which are by nature heterogeneous, the implications are that, if a large enough stress heterogeneity exists, nucleation of a runaway dynamic event can be delayed until the nucleating patch grows past this heterogeneity and dynamic rupture can be halted if one of these heterogeneous stress patches is encountered. Fault roughness is often seen as a proxy for stress heterogeneity, such that smoother surfaces exhibit a more homogeneous stress field (e.g., Cattania & Segall, 2021). McLaskey and Lockner (2014) showed experimentally that acoustic emissions which encountered a roughness-induced stress barrier could have their propagation halted. Similarly, large-roughness-induced normal stress barriers have been shown numerically to induce rupture arrest (Cattania & Segall, 2021). Further, rougher faults have shown less tendency to nucleate a dynamic event under otherwise similar conditions (Harbord et al., 2017).

Recent work has indicated that the nucleation length in these heterogeneous cases will depend on the typical size of the heterogeneity compared to its individual nucleation length,  $a_{\text{nuc}}^{\text{het}}$ , and the average nucleation length,  $a_{\text{nuc}}^{\text{mean}}$ , along the fault. In the limit of large production times, these length scales can be written as

$$a_{\text{nuc}}^{\text{het}} = 0.579 \frac{\mu^*}{w_{\text{het}}(\sigma_0^* - \Delta P_p)}, \text{ and } a_{\text{nuc}}^{\text{mean}} = 0.579 \frac{\mu^*}{w_{\text{mean}}(\sigma_0^* - \Delta P_p)}, \quad (26)$$

where  $w_{\text{het}}$  is the weakening rate of the heterogeneity and  $w_{\text{mean}}$  the average weakening rate along the fault. If the size of the heterogeneity is smaller than the local nucleation length, a dynamic event may initiate from the defect when the aseismic patch reaches this location. In contrast, heterogeneities of scale larger than the average nucleation length are susceptible to modify its overall stability (Lebihain, Roch, Violay, et al., 2022). As such, a preconditioning production phase may promote micro-seismicity through a decrease of  $a_{\text{nuc}}^{\text{het}}$  with increasing  $-\Delta P_p$ , as nucleation length has been seen experimentally to decrease with increasing normal stress (e.g., Cappa et al., 2019; Latour et al., 2013). Nonetheless, the associated decrease in stress drop could halt these “small,” and so less energetic, ruptures. A second effect of preconditioning would be to modify the overall nucleation behavior of the fault, as more and more heterogeneity scales are being involved in the fault stability when the average nucleation length  $a_{\text{nuc}}^{\text{mean}}$  decreases. However, in this investigation, preconditioned faults reached generally larger slip levels at smaller slip rates during injection, so that a larger portion of the slipping patch could achieve residual friction. The existence of a region achieving residual strength near the wellbore increases the average nucleation length, which in turn makes the nucleation behavior of the fault more homogeneous.

Interestingly, in terms of large-scale stress heterogeneity, these results also imply that contained rupture during stimulation may also be achievable by targeting the most optimally oriented sections of fault planes in the case that the orientation of the fault plane shifts to a sub-optimal orientation over an acceptably short distance. The sub-optimally oriented fault sections would need to present a significant enough barrier to halt rupture, however.

## 4.5. Limiting Assumptions

### 4.5.1. Linear Slip-Weakening Model

A number of previous studies have considered similar injection-induced seismicity problems with slip-neutral friction (Bhattacharya & Viesca, 2019; Sáez et al., 2022; Viesca, 2022). Other studies, such as this one, opt for linear slip-weakening models (Ciardo & Lecampion, 2019; Garagash & Germanovich, 2012; Uenishi & Rice, 2003; Viesca & Rice, 2012). A third set of studies instead implement rate-and-state friction frameworks (Dublanche, 2019; Garagash, 2021). The choice of friction model clearly has a large impact on the ultimate behavior of the modeled fault. Slip-neutral models result in aseismic slip and are unable to produce dynamic events. However, they are more tractable than the other models, lending themselves to analytical solutions. Linear slip-weakening models are able to produce richer behavior, including dynamic events, but it is more difficult to find analytical solutions capturing their behavior and they are unable to reproduce the healing and multi-stage weakening behavior seen, for example, in laboratory experiments and on real faults. This is particularly relevant as multiple weakening stages can result in ruptures overcoming stress barriers they otherwise would not have been able to (Paglialunga et al., 2022). They are therefore unable to reproduce the entire seismic cycle. Note, however, that these secondary weakening mechanisms are less likely to occur in the context of preconditioning as they are often controlled by slip rate (Di Toro et al., 2010; Niemeijer et al., 2011; Rice, 2006), which has been shown here to be decreased when preconditioning is employed. Finally, rate-and-state friction models, while empirical in nature, include fault healing and are therefore able to reproduce the entire seismic cycle. Most often, however, rate-and-state friction models must be solved numerically. The friction model implemented depends on the goal of the study and, for field applications, the specific fault being evaluated. Clearly, the results of any study will significantly vary depending on the friction model used.

### 4.5.2. Constant Permeability

In order for the pressure diffusion equation to be solved analytically for two injection rates, permeability must remain constant and homogeneous such that the pressure diffusion equation remains linear. Practically, however, this will not be the case. Other than natural heterogeneities, permeability is also likely to decrease as pore pressure decreases (e.g., Acosta et al., 2020; Lee & Cho, 2002) due to permeability's dependence on effective normal stress. This will make achieving the targeted pore pressure reductions more difficult as they will require more time to achieve. Further, shear stimulation is employed to increase the permeability (Evans, Genter, & Sausse, 2005; Evans, Moriya, et al., 2005; Lee & Cho, 2002), meaning permeability will change during injection. Previous similar works have considered these kinds of permeability changes (Ciardo & Lecampion, 2019; Viesca & Rice, 2012).

#### 4.5.3. Quasi-Static Equilibrium

Earthquakes can be difficult to model as their slow-slipping quasi-static phase lasts many orders of time longer than the dynamic phase which occurs when instability starts. Previous attention has been paid to how to appropriately model these kinds of problems (Lapusta et al., 2000). Here, however, a purely quasi-static approach has been chosen. For this reason, the runaway dynamic events are not modeled past their nucleation phase. Therefore, no insights can be provided into the sizes of the runaway dynamic events occurring with or without preconditioning. Regarding the dynamic overshoot that can occur during crack arrest, Viesca and Rice (2012) showed that rupture is arrested near the conditions predicted from the quasi-static solution in the case of limited slip weakening.

#### 4.5.4. 1-D Fault, Constant Pressure

The model implemented here is a 2-D model for a 1-D fault loaded with constant pressure, corresponding to a line-source injection. In the field, wells are unlikely to be drilled parallel to a fault, intersecting it. Previous works have shown that both the injection scenario considered (Garagash & Germanovich, 2012) and the 2-D assumption (Sáez et al., 2022) have a qualitative impact on the results found. Stimulation treatments are often performed on a 3-D fault at a set rate (e.g., Häring et al., 2008), not a set pressure. For this reason, the results shown here in their details are not directly translatable to a field case. However, this model still allows for the presentation of the technique of pore-pressure preconditioning in a specific example geometry as well as for the demonstration of how, with this technique, both the fracture energy can be increased and energy available to a propagating rupture can be reduced such that the characteristics of earthquake nucleation are altered. The extension to a more realistic 2-D or 3-D fault would alter the required period of preconditioning; however, it is likely that the required production magnitude, Equation 21, would be unchanged.

One may extend the developments presented here to a 2-D planar fault embedded in a 3-D host medium, building on the work of Gao (1988). Using a perturbation method of linear elastic fracture mechanics, their model predicts the change in the modes II and III stress intensity factors and slip distribution arising from a small perturbation of a crack front from its reference circular configuration. This should provide the necessary ingredients to construct a three-dimensional s.s.y. model that describes the propagation of quasi-elliptical shear cracks (Sáez et al., 2022) from the resolution of the axisymmetric problem of a circular fluid-driven rupture. The latter can be solved at a computational cost similar to the 2-D model described here. The proposed s.s.y. model could only describe the propagation phase of shear ruptures above the cohesive length scale  $a_w^*$ . Description of the failure process involved in ruptures smaller than  $a_w^*$  may be built upon the perturbation of crack face weight functions recently proposed by Lebihain, Roch, and Molinari (2022).

#### 4.5.5. Inwardly Propagating Ruptures

Due to the simple nature of the model used here, the center of any nucleated dynamic event is at the wellbore. Note, however, that while induced-seismic events do not necessarily nucleate at the wellbore, and have even been seen to propagate back toward the wellbore (Folesky et al., 2016), laboratory studies have indicated that dynamic rupture seems to initiate within an aseismically slipping patch caused by pore pressure increase (e.g., Cebry et al. (2022)). As sufficient pore-pressure preconditioning causes the aseismically slipping front to remain behind the pore-pressure barrier, a dynamic event would have to nucleate behind this barrier. As demonstrated, ruptures nucleating behind the barrier are contained by it due to a reduced energy available to fuel the rupture and an increased fracture energy. However, ruptures can still propagate inwardly in the region behind the barrier. Indeed, as shown in Section 4.2.1, preconditioning may even result in contained ruptures that are larger than those achievable without preconditioning. For this reason, it may be preferable to avoid using preconditioning to target excessively large stimulation areas. Further, it may be possible to combine other stimulation techniques, such as cyclic stimulation, with preconditioning. In this way, preconditioning would act as a far-field safety net and promote extended periods of aseismic slip. At the same time, employing cyclic stimulation, or even short-term fluid production, during the injection phase would further limit the rupture velocity within the aseismically growing stimulated area.

### 5. Conclusion

Considering that industrial activities can induce both spatial and temporal heterogeneities in the state of stress along a fault, a methodology has been proposed whereby a stress and fracture energy barrier is created through

the production of pore fluid before injection into a fault. This barrier has been shown, through the extension of a model by Garagash and Germanovich (2012), to be potentially capable of delaying dynamic rupture nucleation and halting dynamic rupture propagation while still inducing slip in a region near the point of injection, allowing for stimulation. With laboratory-scale and meso-scale followed by pilot-scale testing, it may be possible to implement this methodology such that operators might stimulate the near-wellbore region of a well without inducing large dynamic shear events. This methodology, while in its infancy, could eventually not only have implications for safe EGS stimulation, but also potentially for the safe release of stress on shallow faults.

## Appendix A

### A1. Scaled Fracture Energy

Beginning with Equation 9, both sides can be normalized by  $f_p$  and  $\sigma_0^*$ ,

$$\frac{G_c}{f_p(S_0 - P_0)} \simeq (1 - \tilde{f}_r) \left( \frac{S_0 - P_0 - P + P_0}{S_0 - P_0} \right) \frac{\delta_r}{2} \quad (\text{A1})$$

which reduces to,

$$\frac{G_c}{f_p(S_0 - P_0)} \simeq (1 - \tilde{f}_r) (1 - \Delta \tilde{P}) \frac{\delta_r}{2}. \quad (\text{A2})$$

Then, considering that for linear slip weakening  $\delta_r = \left( \frac{f_p - f_r}{f_p} \right) \delta_w^*$ ,  $\delta_r$  can be written as,

$$\delta_r = \left( \frac{f_p - f_r}{f_p} \right) \frac{a_w^* \tau^p}{\mu^*}. \quad (\text{A3})$$

This then results in

$$\frac{2G_c \mu^*}{f_p(S_0 - P_0) a_w^*} \simeq (1 - \tilde{f}_r)^2 (1 - \Delta \tilde{P}) \tau^p. \quad (\text{A4})$$

Then,  $\tau^p$  can be replaced,

$$\frac{2G_c \mu^*}{f_p(S_0 - P_0) a_w^*} \simeq (1 - \tilde{f}_r)^2 (1 - \Delta \tilde{P}) f_p(S_0 - P_0 - P + P_0). \quad (\text{A5})$$

Normalizing this equation by  $\sigma_0^*$  and  $f_p$  yields,

$$\frac{2G_c \mu^*}{f_p^2(S_0 - P_0)^2 a_w^*} \simeq (1 - \tilde{f}_r)^2 (1 - \Delta \tilde{P})^2. \quad (\text{A6})$$

### A2. Variable Summaries

Tables A1–A3 provide a list of variables and a short description to aid in reading.

Table A1 General Roman Variable Summary Table	
Variable	Brief description
$a$	Crack length
$a_a$	Crack length at arrest
$a_{\text{nuc}}^{\text{het}}$	Individual nucleation length
$a_{\text{nuc}}^{\text{mean}}$	Average nucleation length
$a_{\text{nuc}}$	Crack length at dynamic-event nucleation
$a_w^*$	Characteristic length
$c_t$	Total compressibility

**Table A1**  
*Continued*

Variable	Brief description
$D$	Diffusivity
$f$	Friction coefficient
$f_p$	Peak friction coefficient
$f_r$	Residual friction coefficient
$G$	Quasi-static energy release rate
$G_c$	Fracture energy
$K$	Stress intensity factor
$k$	Permeability
$M_0$	Seismic moment
$P$	Pressure
$P_0$	Initial pressure
$q$	Injection rate
$\Delta P$	Net pressure
$\Delta P_i$	Net injection pressure
$\Delta P_p$	Net production pressure
$S_0$	Total normal stress
$t$	Injection time
$t^*$	Characteristic time
$t_p$	Production time
$w$	Linear slip-weakening coefficient
$x$	Location

*Note.* The general Roman variables used during the study as well as a brief description

**Table A2**  
*General Greek Variable Summary Table*

Variable	Brief description
$\delta$	Slip
$\delta_{nuc}$	Slip at dynamic-event nucleation
$\delta_f$	Slip during foreshock
$\delta_r$	Slip slip to achieve residual friction
$\delta_w^*$	Characteristic slip
$\eta$	Fluid dynamic viscosity
$\mu$	Shear modulus
$\mu^*$	Equivalent shear modulus
$\nu$	Poisson's ratio
$\sigma$	Effective normal stress
$\sigma_0^*$	Characteristic stress
$\tau$	Shear stress
$\tau^b$	Background shear stress
$\tau^p$	Peak shear stress
$\tau^r$	Residual shear stress
$\Phi$	Porosity

*Note.* The general Greek variables used during the study as well as a brief description



**Table A3**

*Normalized Variable Summary Table*

Variable	Brief description
$\tilde{a}$	Normalized crack length
$\tilde{a}_a$	Normalized crack length at arrest
$\tilde{a}_{nuc}$	Normalized crack length at dynamic-event nucleation
$\tilde{f}_r$	Normalized residual friction
$\tilde{G}$	Normalized fracture energy
$\tilde{K}$	Normalized stress intensity factor
$\tilde{M}_0$	Normalized seismic moment
$\Delta \tilde{P}$	Normalized net pressure
$\Delta \tilde{P}_i$	Normalized net injection pressure
$\Delta \tilde{P}_p$	Normalized net production pressure
$\tilde{t}$	Normalized injection time
$\tilde{t}_p$	Normalized production time
$\tilde{x}$	Normalized horizontal location along fault
$\tilde{x}_b$	Normalized barrier-in-space location along fault
$\tilde{x}_t$	Normalized barrier-in-time location along fault
$\tilde{\delta}$	Normalized slip
$\tilde{\delta}_{nuc}$	Normalized slip at dynamic-event nucleation
$\tilde{\delta}_f$	Normalized slip during foreshock
$\tilde{\delta}_r$	Normalized slip to achieve residual friction
$\tilde{\tau}$	Normalized stress criticality
$\tilde{\tau}^b$	Normalized background stress

*Note.* The normalized variables used during the study as well as a brief description.

## Conflict of Interest

The authors declare no conflicts of interest relevant to this study.

## Data Availability Statement

The Python code used to produce the data as well as the data that is plotted in the figures has been made available online (Fryer et al., 2022).

## Acknowledgments

BF, ML, and MV acknowledge support from the European Research Council Starting Grant project 757290-BEFINE. The authors would like to gratefully acknowledge their insightful discussions with Alexis Sáez, especially regarding the analytical pore pressure model. The authors are grateful for the helpful comments provided by the editors and two reviewers. Open access funding provided by the Ecole Polytechnique Fédérale de Lausanne.

## References

- Abercrombie, R., & Mori, J. (1996). Occurrence patterns of foreshocks to large earthquakes in the western United States. *Nature*, 381(6580), 303–307. <https://doi.org/10.1038/381303a0>
- Acosta, M., Maye, R., & Violay, M. (2020). Hydraulic transport through calcite bearing faults with customized roughness: Effects of normal and shear loading. *Journal of Geophysical Research: Solid Earth*, 125(8), e2020JB019767. <https://doi.org/10.1029/2020JB019767>
- Aki, K., & Richards, P. (2009). *Quantitative seismology*. University Science Books.
- Ampuero, J., Ripperger, J., & Mai, P. (2006). Properties of dynamic earthquake ruptures with heterogeneous stress drop. *Earthquakes: Radiated Energy and the Physics of Faulting*, 170, 255–261. <https://doi.org/10.1029/170GM25>
- Baria, R., Michelet, S., Baumgaertner, J., Dyer, B., Gerard, A., Nicholls, J., et al. (2004). Microseismic monitoring of the World's largest potential HDR reservoir. *Paper presented at Twenty-ninth Workshop on Geothermal Reservoir Engineering*. Stanford University.
- Bayart, E., Svetlizky, I., & Fineberg, J. (2016). Fracture mechanics determine the lengths of interface ruptures that mediate frictional motion. *Nature Physics*, 12(2), 166–170. <https://doi.org/10.1038/nphys3539>
- Bayart, E., Svetlizky, I., & Fineberg, J. (2018). Rupture dynamics of heterogeneous frictional interfaces. *Journal of Geophysical Research: Solid Earth*, 123(5), 3828–3848. <https://doi.org/10.1002/2018JB015509>
- Berchenko, I., & Detournay, E. (1997). Deviation of hydraulic fractures through poroelastic stress changes induced by fluid injection and pumping. *International Journal of Rock Mechanics and Mining Sciences*, 34(6), 1009–1019. [https://doi.org/10.1016/S1365-1609\(97\)80010-X](https://doi.org/10.1016/S1365-1609(97)80010-X)

- Bhattacharya, P., & Viesca, R. (2019). Fluid-induced aseismic fault slip outpaces pore-fluid migration. *Science*, 364(6439), 464–468. <https://doi.org/10.1126/science.aaw7354>
- Bilby, B., & Eshelby, J. (1968). Dislocations and the theory of fracture. In H. Liebowitz (Ed.), *Fracture, an advanced treatise* (pp. 99–182). Academic.
- Bouteca, M., Lessi, J., & Sarda, J. (1983). Stress changes induced by fluid injection in a porous layer around a wellbore. *Paper presented at 24th U.S. Symposium on Rock Mechanics*.
- Cappa, F., Scuderi, M., Colletini, C., Guglielmi, Y., & Avouac, J. (2019). Stabilization of fault slip by fluid injection in the laboratory and in situ. *Science Advances*, 5(3), eaau4065. <https://doi.org/10.1126/sciadv.aau4065>
- Carslaw, H., & Jaeger, J. (1959). *Conduction of heat in solids*. Oxford University Press.
- Catalli, F., Meier, M., & Wiemer, S. (2013). The role of Coulomb stress changes for injection-induced seismicity: The Basel enhanced geothermal system. *Geophysical Research Letters*, 40(1), 72–77. <https://doi.org/10.1029/2012GL054147>
- Catalli, F., Rinaldi, A., Gischig, V., Nespola, M., & Wiemer, S. (2016). The importance of earthquake interactions for injection-induced seismicity: Retrospective modeling of the Basel Enhanced Geothermal System. *Geophysical Research Letters*, 43(10), 4992–4999. <https://doi.org/10.1002/2016GL068932>
- Cattania, C., & Segall, P. (2021). Precursory slow slip and foreshocks on rough faults. *Journal of Geophysical Research: Solid Earth*, 126(4), e2020JB020430. <https://doi.org/10.1029/2020JB020430>
- Cebry, S., Ke, C., & McLaskey, G. (2022). The role of background stress state in fluid-induced aseismic slip and dynamic rupture on a 3-m laboratory fault. *Journal of Geophysical Research: Solid Earth*, 127(8), e2022JB024371. <https://doi.org/10.1029/2022JB024371>
- Cebry, S., & McLaskey, G. (2021). Seismic swarms produced by rapid fluid injection into a low permeability laboratory fault. *Earth and Planetary Science Letters*, 557, 116726. <https://doi.org/10.1016/j.epsl.2020.116726>
- Ciardo, F., & Lecampion, B. (2019). Effect of dilatancy on the transition from aseismic to seismic slip due to fluid injection in a fault. *Journal of Geophysical Research: Solid Earth*, 124(4), 3724–3743. <https://doi.org/10.1029/2018JB016636>
- Ciardo, F., & Rinaldi, A. (2022). Impact of injection rate ramp-up on nucleation and arrest of dynamic fault slip. *Geomechanics and Geophysics for Geo-Energy and Geo-Resources*, 8(1), 28. <https://doi.org/10.1007/s40948-021-00336-4>
- Cornet, F. (2019). The engineering of safe hydraulic stimulations for EGS development in hot crystalline rock masses. *Geomechanics for Energy and the Environment*, 26, 100151. <https://doi.org/10.1016/j.gete.2019.100151>
- Dake, L. (1978). *Fundamentals of reservoir engineering*. Elsevier Science.
- Di Toro, G., Niemeijer, A., Tirpoli, A., Nielsen, S., Di Felice, F., Scarlato, P., et al. (2010). From field geology to earthquake simulation: A new state-of-the-art tool to investigate rock friction during the seismic cycle (SHIVA). *Rendiconti Lincei. Scienze Fisiche e Naturali*, 21(S1), 95–114. <https://doi.org/10.1007/s12210-010-0097-x>
- Dieterich, J. (1972). Time-dependent friction in rocks. *Journal of Geophysical Research*, 77(20), 3690–3697. <https://doi.org/10.1029/JB077i020p03690>
- Dohmen, T., Blangy, J., & Zhang, J. (2014). Microseismic depletion delineation. *Interpretation*, 2(3), SG1–SG13. <https://doi.org/10.1190/INT-2013-0164.1>
- Dohmen, T., Zhang, J., Barker, L., & Blangy, J. (2017). Microseismic magnitudes and b-values for delineating hydraulic fracturing and depletion. *SPE Journal*, 22(5), 1624–1634. <https://doi.org/10.2118/186096-PA>
- Dohmen, T., Zhang, J., Li, C., Blangy, J., Simon, K., Valteau, D., et al. (2013). A new surveillance method for delineation of depletion using microseismic and its application to development of unconventional reservoirs. *Paper presented at SPE Annual Technical Conference and Exhibition*. Society of Petroleum Engineers. <https://doi.org/10.2118/166274-MS>
- Dublanche, P. (2019). Fluid driven shear cracks on a strengthening rate-and-state frictional fault. *Journal of the Mechanics and Physics of Solids*, 132, 103672. <https://doi.org/10.1016/j.jmps.2019.07.015>
- Elbel, J., & Mack, M. (1993). Refracturing: Observations and theories. *Paper presented at SPE Production Operations Symposium*.
- Evans, K., Genter, A., & Sausse, J. (2005). Permeability creation and damage due to massive fluid injections into granite at 3.5 km at Soultz 1. Borehole observations. *Journal of Geophysical Research*, 110(B4), B04203. <https://doi.org/10.1029/2004JB003168>
- Evans, K., Moriya, H., Niitsuma, H., Jones, R., Phillips, W., Genter, A., et al. (2005). Microseismicity and permeability enhancement of hydrogeologic structures during massive fluid injections into granite at 3 km depth at the Soultz HDR site. *Geophysical Journal International*, 160(1), 388–412. <https://doi.org/10.1111/j.1365-246X.2004.02474.x>
- Evans, K., Zappone, A., Kraft, T., Deichmann, N., & Moia, F. (2012). A survey of the induced seismic responses to fluid injection in geothermal and CO<sub>2</sub> reservoirs in Europe. *Geothermics*, 41, 30–54. <https://doi.org/10.1016/j.geothermics.2011.08.002>
- Fisher, M., Heinze, J., Harris, C., Davidson, B., Wright, C., & Dunn, K. (2004). Optimizing horizontal completion techniques in the Barnett Shale using microseismic fracture mapping. *Paper presented at SPE Annual Technical Conference and Exhibition*.
- Folesky, J., Kummerow, J., Shapiro, S., Häring, M., & Asanuma, H. (2016). Rupture directivity of fluid-induced microseismic events: Observations from an enhanced geothermal system. *Journal of Geophysical Research: Solid Earth*, 121(11), 8034–8047. <https://doi.org/10.1002/2016JB013078>
- Freund, L. (1998). *Dynamic fracture mechanics*. Cambridge University Press.
- Fryer, B., Lebihain, M., & Violay, M. (2022). Data set: Single-well pore pressure preconditioning for enhanced geothermal system stimulation [Dataset]. Zenodo. <https://doi.org/10.5281/zenodo.7492868>
- Fryer, B., Siddiqi, G., & Laloui, L. (2020). Injection-induced seismicity: Strategies for reducing risk using high stress path reservoirs and temperature-induced stress preconditioning. *Geophysical Journal International*, 220(2), 1436–1446. <https://doi.org/10.1093/gji/gg2490>
- Galís, M., Ampuero, J., Mai, P., & Cappa, F. (2017). Induced seismicity provides insight into why earthquake ruptures stop. *Science Advances*, 3(12), eaap7528. <https://doi.org/10.1126/sciadv.aap7528>
- Gao, H. (1988). Nearly circular shear mode cracks. *International Journal of Solids and Structures*, 24(2), 177–193. [https://doi.org/10.1016/0020-7683\(88\)90028-5](https://doi.org/10.1016/0020-7683(88)90028-5)
- Gao, Q., Cheng, Y., Han, S., Yan, C., & Jiang, L. (2019). Numerical modeling of hydraulic fracture propagation behaviors influenced by pre-existing injection and production wells. *Journal of Petroleum Science and Engineering*, 172, 976–987. <https://doi.org/10.1016/j.petrol.2018.09.005>
- Garagash, D. (2021). Fracture mechanics of rate-and-state faults and fluid injection induced slip. *Philosophical Transactions of the Royal Society A*, 379(2196), 20200129. <https://doi.org/10.1098/rsta.2020.0129>
- Garagash, D., & Germanovich, L. (2012). Nucleation and arrest of dynamic slip on a pressurized fault. *Journal of Geophysical Research*, 117(B10), B10310. <https://doi.org/10.1029/2012JB009209>

- Gischig, V. (2015). Rupture propagation behavior and the largest possible earthquake induced by fluid injection into deep reservoirs. *Geophysical Research Letters*, 42(18), 7420–7428. <https://doi.org/10.1002/2015GL065072>
- Goertz-Allmann, B., Goertz, A., & Wiemer, S. (2011). Stress drop variations of induced earthquakes at the Basel geothermal site. *Geophysical Research Letters*, 38(9), L09308. <https://doi.org/10.1029/2011GL047498>
- Grigoli, F., Cesca, S., Rinaldi, A., Manconi, A., López-Comino, J., Clinton, J., et al. (2018). The November 2017 Mw 5.5 Pohang earthquake: A possible case of induced seismicity in South Korea. *Science*, 360(6392), 1003–1006. <https://doi.org/10.1126/science.aat2010>
- Guglielmi, Y., Cappa, F., Avouac, J., Henry, P., & Elsworth, D. (2015). Seismicity triggered by fluid injection-induced aseismic slip. *Science*, 348(6240), 1224–1226. <https://doi.org/10.1126/science.aab0476>
- Gupta, A., & Scholz, C. (2000). A model of normal fault interaction based on observations and theory. *Journal of Structural Geology*, 22(7), 865–879. [https://doi.org/10.1016/S0191-8141\(00\)00011-0](https://doi.org/10.1016/S0191-8141(00)00011-0)
- Gvirtsman, S., & Fineberg, J. (2021). Nucleation fronts ignite the interface rupture that initiates frictional motion. *Nature Physics*, 17(9), 1037–1042. <https://doi.org/10.1038/s41567-021-01299-9>
- Harbord, C., Nielsen, S., De Paola, N., & Holdsworth, R. (2017). Earthquake nucleation on rough faults. *Geology*, 45(10), 931–934. <https://doi.org/10.1130/G39181.1>
- Häring, M., Schanz, U., Ladner, F., & Dyer, B. (2008). Characterisation of the Basel 1 enhanced geothermal system. *Geothermics*, 37(5), 469–495. <https://doi.org/10.1016/j.geothermics.2008.06.002>
- Harrison, E., Kieschnick, W., & McGuire, W. (1954). The mechanics of fracture induction and extension. *Petroleum Transactions*, 201(1), 252–263. <https://doi.org/10.2118/318-g>
- Healy, J., Rubey, W., Griggs, D., & Raleigh, C. (1968). The Denver earthquakes. *Science*, 161(3848), 1301–1310. <https://doi.org/10.1126/science.161.3848.1301>
- Hofmann, H., Zimmermann, G., Farkas, M., Huenges, E., Zang, A., Leonhardt, M., et al. (2019). First field application of cyclic soft stimulation at the Pohang Enhanced Geothermal System site in Korea. *Geophysical Journal International*, 217(2), 926–949. <https://doi.org/10.1093/gji/ggz058>
- Hofmann, H., Zimmermann, G., Huenges, E., Regenspurg, S., Aldaz, S., Milkereit, C., et al. (2021). Soft stimulation treatment of geothermal well RV-43 to meet the growing heat demand of Reykjavik. *Geothermics*, 96, 102146. <https://doi.org/10.1016/j.geothermics.2021.102146>
- Hofmann, H., Zimmermann, G., Zang, A., & Min, K. (2018). Cyclic soft stimulation (CSS): A new fluid injection protocol and traffic light system to mitigate seismic risks of hydraulic stimulation treatments. *Geothermal Energy*, 6(1), 27. <https://doi.org/10.1186/s40517-018-0114-3>
- Husseini, M., Jovanovich, D., Randall, M., & Freund, L. (1975). The fracture energy of earthquakes. *Geophysical Journal International*, 43(2), 367–385. <https://doi.org/10.1111/j.1365-246X.1975.tb00640.x>
- Ida, Y. (1972). Cohesive force across the tip of a longitudinal-shear crack and Griffith's specific surface energy. *Journal of Geophysical Research*, 77(20), 3796–3805. <https://doi.org/10.1029/JB077i020p03796>
- Jacquey, A., & Viesca, R. (2022). Nucleation and arrest of fluid-induced aseismic slip. *ESSOAr*. <https://doi.org/10.1002/essoar.10512431.1>
- Johann, L., Dinske, C., & Shapiro, S. (2016). Scaling of seismicity induced by nonlinear fluid-rock interaction after an injection stop. *Journal of Geophysical Research: Solid Earth*, 121(11), 8154–8174. <https://doi.org/10.1002/2016JB012949>
- Kammer, D., Radiguet, M., Ampuero, J., & Molinari, J. (2015). Linear elastic fracture mechanics predicts the propagation distance of frictional slip. *Tribology Letters*, 57(3), 23. <https://doi.org/10.1007/s11249-014-0451-8>
- Ke, C., McLaskey, G., & Kammer, D. (2018). Rupture termination in laboratory-generated earthquakes. *Geophysical Research Letters*, 45(23), 12784–12792. <https://doi.org/10.1029/2018GL080492>
- Ke, C., McLaskey, G., & Kammer, D. (2021). The earthquake arrest zone. *Geophysical Journal International*, 224(1), 581–589. <https://doi.org/10.1093/gji/ggaa386>
- Kim, K., Ree, J., Kim, Y., Kim, S., Kang, S., & Seo, W. (2018). Assessing whether the 2017  $M_w$  5.4 Pohang earthquake in South Korea was an induced event. *Science*, 360(6392), 1007–1009. <https://doi.org/10.1126/science.aat6081>
- King, G. (1986). Speculations on the geometry of the initiation and termination processes of earthquake rupture and its relation to morphology and geological structure. *Pure and Applied Geophysics*, 124(3), 567–585. <https://doi.org/10.1007/BF00877216>
- Kumar, D., & Ghassemi, A. (2019). Multistage hydraulic fracturing of EGS wells with application to FORGE. *Paper presented at Proceedings, 44th Workshop on Geothermal Reservoir Engineering*. Stanford University.
- Kwiatek, G., Bohnhoff, M., Dresen, G., Schulze, A., Schulte, T., Zimmermann, G., & Huenges, E. (2008). Microseismicity induced during fluid-injection: A case study from the geothermal site at Groß Schönebeck, North German Basin. *Acta Geophysica*, 58(6), 995–1020. <https://doi.org/10.2478/s11600-010-0032-7>
- Kwiatek, G., Martínez-Garzón, P., Dresen, G., Bohnhoff, M., Sone, H., & Hartline, C. (2015). Effects of long-term fluid injection on induced seismicity parameters and maximum magnitude in northwestern part of The Geysers geothermal field. *Journal of Geophysical Research: Solid Earth*, 120(10), 7085–7101. <https://doi.org/10.1002/2015JB012362>
- Lapusta, N., Rice, J., Ben-Zion, Y., & Zheng, G. (2000). Elastodynamic analysis for slow tectonic loading with spontaneous rupture episodes on faults with rate-and-state dependent friction. *Journal of Geophysical Research*, 105(B10), 23765–23789. <https://doi.org/10.1029/2000JB900250>
- Laroche, S., Lapusta, N., Ampuero, J., & Cappa, F. (2021). Constraining fluid friction and stability with fluid-injection field experiments. *Geophysical Research Letters*, 48(10), e2020GL091188. <https://doi.org/10.1029/2020GL091188>
- Latour, S., Schubnel, A., Nielsen, S., Madariaga, R., & Vinciguerra, S. (2013). Characterization of nucleation during laboratory earthquakes. *Geophysical Research Letters*, 40(19), 5064–5069. <https://doi.org/10.1002/grl.50974>
- Lay, T., & Kanamori, H. (1981). An asperity model of large earthquake sequences. In *Earthquake prediction* (pp. 579–592). AGU.
- Lebihain, M., Roch, T., & Molinari, J. (2022). Quasi-static crack front deformations in cohesive materials. *Journal of the Mechanics and Physics of Solids*, 168, 105025. <https://doi.org/10.1016/j.jmps.2022.105025>
- Lebihain, M., Roch, T., Violay, M., & Molinari, J. (2022). Earthquake nucleation along faults with heterogeneous weakening rate. *Geophysical Research Letters*, 48(21), e2021GL094901. <https://doi.org/10.1029/2021GL094901>
- Lee, H., & Cho, T. (2002). Hydraulic characteristics of rough fractures in linear flow under normal and shear load. *Rock Mechanics and Rock Engineering*, 35(4), 299–318. <https://doi.org/10.1007/s00603-002-0028-y>
- Leeman, J., Saffer, D., Scuderi, M., & Marone, C. (2016). Laboratory observations of slow earthquakes and the spectrum of tectonic fault slip modes. *Nature Communications*, 7(1), 11104. <https://doi.org/10.1038/ncomms11104>
- McClure, M., & Horne, R. (2014). An investigation of stimulation mechanisms in Enhanced Geothermal Systems. *International Journal of Rock Mechanics and Mining Sciences*, 72, 242–260. <https://doi.org/10.1016/j.ijrmms.2014.07.011>
- McLaskey, G., & Lockner, D. (2014). Preslip and cascade processes initiating laboratory stick slip. *Journal of Geophysical Research: Solid Earth*, 119(8), 6323–6336. <https://doi.org/10.1002/2014JB011220>

- Meier, P., Rodríguez, A., & Bethmann, F. (2015). Lessons learned from Basel: New EGS projects in Switzerland using multistage stimulation and a probabilistic traffic light system for the reduction of seismic risk. *Paper presented at Proceedings World Geothermal Congress 2015*.
- Minner, W., Wright, C., Stanley, G., de Pater, C., Gorham, T., Eckerfield, L., & Hejl, K. (2002). Waterflood and production-induced stress changes dramatically affect hydraulic fracture behavior in Lost Hills infill wells. *Paper presented at SPE Annual Technical Conference and Exhibition*.
- National-Research-Council. (2013). *Induced seismicity potential in energy technologies*. The National Academies Press. <https://doi.org/10.1726/13355>
- Niemeijer, A., Di Toro, G., Nielsen, S., & Di Felice, F. (2011). Frictional melting of gabbro under extreme experimental conditions of normal stress, acceleration, and sliding velocity. *Journal of Geophysical Research*, 116(B7), B07404. <https://doi.org/10.1029/2010JB008181>
- Noël, C., Pimienta, L., & Violay, M. (2019). Time-dependent deformations of sandstone during pore fluid pressure oscillations: Implications for natural and induced seismicity. *Journal of Geophysical Research: Solid Earth*, 124(1), 801–821. <https://doi.org/10.1029/2018JB016546>
- Norbeck, J., & Horne, R. (2015). Physical mechanisms related to microseismic-depletion-delineation field tests with application to reservoir surveillance. *SPE Journal*, 21(4), 1279–1288. <https://doi.org/10.2118/178926-PA>
- Norbeck, J., McClure, M., & Horne, R. (2018). Field observations at the Fenton Hill enhanced geothermal system test site support mixed-mechanism stimulation. *Geothermics*, 74, 135–149. <https://doi.org/10.1016/j.geothermics.2018.03.003>
- Okubo, P., & Dieterich, J. (1984). Effects of physical fault properties on frictional instabilities produced on simulated faults. *Journal of Geophysical Research*, 89(B7), 5817–5827. <https://doi.org/10.1029/jb089ib07p05817>
- Pagliialunga, F., Passelègue, F., Brantut, N., Barras, F., Lebihain, M., & Violay, M. (2022). On the scale dependence in the dynamics of frictional rupture: Constant fracture energy versus size-dependent breakdown work. *Earth and Planetary Science Letters*, 584, 117442. <https://doi.org/10.1016/j.epsl.2022.117442>
- Palmer, A., & Rice, J. (1973). The growth of slip surfaces in the progressive failure of over-consolidated clay. *Proceedings of the Royal Society of London. Series A*, 332, 527–548. <https://doi.org/10.1098/rspa.1973.0040>
- Passelègue, F., Almakari, M., Dublanche, P., Barras, F., Fortin, J., & Violay, M. (2020). Initial effective stress controls the nature of earthquakes. *Nature Communications*, 11(1), 5132. <https://doi.org/10.1038/s41467-020-18937-0>
- Passelègue, F., Aubry, J., Nicolas, A., Fondriest, M., Deldicque, D., Schubnel, A., & Di Toro, G. (2019). From fault creep to slow and fast earthquakes in carbonates. *Geology*, 47(8), 744–748. <https://doi.org/10.1130/G45868.1>
- Raleigh, C., Healy, J., & Bredehoeft, J. (1976). An experiment in earthquake control at Rangely, Colorado. *Science*, 191(4233), 1230–1237. <https://doi.org/10.1126/science.191.4233.1230>
- Rice, J. (1968a). Mathematical analysis in the mechanics of fracture. In H. Liebowitz (Ed.), *Fracture: An advanced treatise* (pp. 191–311). Academic Press.
- Rice, J. (1968b). A path independent integral and the approximate analysis of strain concentration by notches and cracks. *Journal of Applied Mechanics*, 35(2), 379–386. <https://doi.org/10.1115/1.3601206>
- Rice, J. (2006). Heating and weakening of faults during earthquake slip. *Journal of Geophysical Research*, 111(B5), B05311. <https://doi.org/10.1029/2005JB004006>
- Roux, A., Leeman, E., & Denkhaus, H. (1957). De-stressing: A means of ameliorating rockburst conditions. Part I—The concept of de-stressing and the results obtained from its application. *Journal of the South African Institute of Mining and Metallurgy*, 59(1), 101–119.
- Rutqvist, J., Jeanne, P., Dobson, P., Garcia, J., Hartline, C., Hutchings, L., et al. (2016). The Northwestern Geysers EGS Demonstration Project, California – Part 2: Modeling and interpretation. *Geothermics*, 63, 120–138. <https://doi.org/10.1016/j.geothermics.2015.08.002>
- Sáez, A., & Lecampion, B. (2022). Post-injection aseismic slip, implications for the delayed and far-reaching triggering of seismicity. arXiv. (arXiv:2211.16803).
- Sáez, A., Lecampion, B., Bhattachary, P., & Viesca, R. (2022). Three-dimensional fluid-driven stable frictional ruptures. *Journal of the Mechanics and Physics of Solids*, 160, 104754. <https://doi.org/10.1016/j.jmps.2021.104754>
- Segall, P. (1989). Earthquakes triggered by fluid extraction. *Geology*, 17(10), 942–946. [https://doi.org/10.1130/0091-7613\(1989\)017<0942:ETBFE>2.3.CO;2](https://doi.org/10.1130/0091-7613(1989)017<0942:ETBFE>2.3.CO;2)
- Segall, P., & Lu, S. (2015). Injection-induced seismicity: Poroelastic and earthquake nucleation effects. *Journal of Geophysical Research: Solid Earth*, 120(7), 5082–5103. <https://doi.org/10.1002/2015JB012060>
- Shapiro, S., Kummerow, J., Dinske, C., Asch, G., Rothert, E., Erzinger, J., et al. (2006). Fluid induced seismicity guided by a continental fault: Injection experiment of 2004/2005 at the German Deep Drilling Site (KTB). *Geophysical Research Letters*, 33(1), L01309. <https://doi.org/10.1029/2005GL024659>
- Shuck, L. (1977). Method for selectively orienting induced fractures in subterranean Earth formations. U.S. Patent No. 4005750.
- Sibson, R. (1985). Stopping of earthquake ruptures at dilational fault jogs. *Nature*, 316(6025), 248–251. <https://doi.org/10.1038/316248a0>
- Suckale, J. (2009). Induced seismicity in hydrocarbon fields. *Advances in Geophysics*, 51, 55–106. [https://doi.org/10.1016/S0065-2687\(09\)05107-3](https://doi.org/10.1016/S0065-2687(09)05107-3)
- Tester, J., Anderson, B., Batchelor, A., Blackwell, D., DiPippo, R., Drake, E., et al. (2006). The future of geothermal energy.
- Toper, A., Kabongo, K., Stewart, R., & Daehnke, A. (2000). The mechanism, optimization and effects of preconditioning. *Journal of the South African Institute of Mining and Metallurgy*, 7–15.
- Uenishi, K., & Rice, J. (2003). Universal nucleation length for slip-weakening rupture instability under nonuniform fault loading. *Journal of Geophysical Research*, 108(B1), 2042. <https://doi.org/10.1029/2001JB001681>
- Valley, B., & Evans, K. (2019). Stress magnitudes in the Basel enhanced geothermal system. *International Journal of Rock Mechanics and Mining Sciences*, 118, 1–20. <https://doi.org/10.1016/j.ijrmms.2019.03.008>
- van Eekelen, H. (1982). Hydraulic fracture geometry: Fracture containment in layered formations. *Society of Petroleum Engineers Journal*, 22(3), 341–349. <https://doi.org/10.2118/9261-PA>
- Vermeylen, J., & Zoback, M. (2011). Hydraulic fracturing, microseismic magnitudes, and stress evolution in the Barnett Shale, Texas, USA. *Paper presented at SPE Hydraulic Fracturing Technology Conference*, The Woodlands.
- Viesca, R. (2022). Self-similar fault slip in response to fluid injection. *Journal of Fluid Mechanics*, 928, A29. <https://doi.org/10.1017/jfm.2021.825>
- Viesca, R., & Rice, J. (2012). Nucleation of slip-weakening rupture instability in landslides by localized increase in pore pressure. *Journal of Geophysical Research*, 117(B3), B03104. <https://doi.org/10.1029/2011JB008866>
- Warpinski, N., & Branagan, P. (1989). Altered-stress fracturing. *Journal of Petroleum Technology*, 41(9), 990–997. <https://doi.org/10.2118/17533-PA>

- Wu, B., & McLaskey, G. (2018). Contained laboratory earthquakes ranging from slow to fast. *Journal of Geophysical Research: Solid Earth*, 124(10), 10270–10291. <https://doi.org/10.1029/2019JB017865>
- Zang, A., Yoon, J., Stephansson, O., & Heidbach, O. (2013). Fatigue hydraulic fracturing by cyclic reservoir treatment enhances permeability and reduces induced seismicity. *Geophysical Journal International*, 195(2), 1282–1287. <https://doi.org/10.1093/gji/ggt301>
- Zimmermann, G., Moeck, I., & Blöcher, G. (2010). Cyclic waterfrac stimulation to develop an Enhanced Geothermal System EGS-Conceptual design and experimental results. *Geothermics*, 39(1), 59–69. <https://doi.org/10.1016/j.geothermics.2009.10.003>